Airborne Measurements of the Wavenumber Spectra of Ocean Surface Waves. Part II: Directional Distribution*

PAUL A. HWANG AND DAVID W. WANG

Oceanography Division, Naval Research Laboratory, Stennis Space Center, Mississippi

EDWARD J. WALSH+ AND WILLIAM B. KRABILL

NASA/GFSC/WFF, Wallops Island, Virginia

ROBERT N. SWIFT

EG&G, WFF, Wallops Island, Virginia

(Manuscript received 12 May 1999, in final form 15 December 1999)

ABSTRACT

An airborne scanning lidar system acquires three-dimensional (3D) spatial topography of ocean surface waves. From the spatial data, wavenumber spectra are computed directly. The spectral properties in terms of the spectral slope and dimensionless spectral coefficient have been verified to be in very good agreement with existing data. One of the unique features of the 3D spatial data is its exceptional directional resolution. Directional properties such as the wavenumber dependence of the directional spreading function and the evolution of bimodal development are investigated with these high-resolution, phase-resolving spatial measurements. Equations for the spreading parameters, the lobe angle, and the lobe ratio are established from the airborne scanning lidar datasets. Fourier decomposition of the measured directional distribution is presented. The directional parameters can be represented by a small number (4) of the Fourier components. The measured directional distributions are compared with numerical experiments of nonlinear wave simulations to explore the functional form of the dissipation source term.

1. Introduction

The study of the directionality of a random wave field is of great interest to the clarification of nonlinear wave dynamics (e.g., Komen et al. 1984; Banner and Young 1994). Traditionally, the directional distribution of waves has been considered unimodal. The most commonly used directional models include cos squared $[\cos^{2s}(\theta/2)]$ (Mitsuyasu et al. 1975; Hasselmann et al. 1980) and sech squared $[\mathrm{sech}^2(b\theta)]$ functions (Donelan et al. 1985; Banner 1990), where θ is the wave propagation angle and parameters s and b are functions of wave frequency and possibly also wave age. These directional distribution models describe a minimal spreading near the peak frequency. Away from the spectral peak, the spreading increases toward both higher and lower frequencies. There are significant disagreements in the wave age dependence among the proposed spectral functions. Detailed comparisons of four distribution models (Mitsuyasu et al. 1975; Hasselmann et al. 1980; Donelan et al. 1985; Banner 1990) have been given in Young (1994) and Ewans (1998) and will not be repeated here. It is generally considered that the characteristics of the directional distribution function reflect the interactive roles played by the source terms (wind generation, breaking dissipation, nonlinear wave–wave interaction) in the action density or spectral energy conservation equation that governs the wave dynamics (Hasselmann et al. 1980; Komen at al. 1984; Donelan et al. 1985). The accurate determination of the directional distribution function thus serves as a diagnostic tool for the quantification of key mechanisms governing the dynamics of ocean waves.

Recently, the existence of bimodal feature in the directional distribution has generated much interest (e.g., Banner and Young 1994; Young et al. 1995; Ewans 1998). Numerical experiments of Komen et al. (1984),

* U.S. Naval Research Laboratory Contribution Number JA/17332-9-0020.

+ Additional affiliation: NOAA/ETL, Boulder, Colorado.

Corresponding author address: Dr. Paul A. Hwang, Oceanography Division, Naval Research Laboratory, Stennis Space Center, MS 39529-5004.
E-mail: paul.hwang@nrlssc.navy.mil

Young and Van Vledder (1993), and Banner and Young (1994) suggest that the directional spreading is controlled mainly by nonlinear interactions. The numerical experiments also reveal that the simulated directional distribution function differs from the standard [cos squared or sech squared] spreading functions, and that bimodal directional distribution develops in the short wave portion of the spectrum. Banner and Young (1994) suggest that bimodal development is caused by the difference in the directional characteristics of wind input and breaking dissipation terms. In particular, the wind input function is more directional (the spreading factor is narrower by a cosine factor) than the dissipation function. As a result, wave components oblique to the wind direction have a net energy loss between the wind input and breaking dissipation terms. Because the three major source terms (wind input, breaking dissipation, and nonlinear interaction) are coupled, the more rapid decay in those oblique components is made up by nonlinear interaction that transfers energy into those components. The issue, however, remains unsettled because disagreement in the interpretation of the observational evidence—the ''existence'' of the bimodal feature in a given dataset turns out to be very much dependent on the processing procedure [e.g., see discussions in Young (1994) and Ewans (1998)].

As mentioned at the beginning of this section, earlier analyses of temporal measurements by wave gauge arrays or directional buoys show unimodal distributions (e.g., Mitsuyasu et al. 1975; Hasselmann et al. 1980; Donelan et al. 1985). Bimodal features have been extracted from temporal measurements only recently, using a maximum likelihood method (MLM) or maximum entropy method (MEM) (Young et al. 1995; Ewans 1998). These results highlight the major difficulty in resolving directional distribution properties from a small number of sensor elements. Depending on the chosen method in the analysis procedure, significant quantitative differences occur. For example, Young (1994) compares the directional resolutions of the Fourier expansion method and the MLM. Considerable broadening of the bimodal feature using either method is illustrated (e.g., Young 1994, Fig. 4). Ewans (1998, Fig. 8) shows a comparison of the bimodal analysis using MLM and MEM. The directional resolution of MEM is much ''sharper,'' although the method was known to produce a false bimodal distribution in tests using synthetic data (Ewans 1998, pp. 503–504; Lyger and Krogstad 1986). Despite these shortcomings, significant progress has been made from the Ewans (1998) MEM analysis. For example, results of the lobe separation angle as a function of dimensionless wave frequency over a wide range of wave age conditions are established from one year of data collected in an offshore station with well-defined fetch conditions. He also shows that the simulation results on the lobe angle based on the EXACT-NL model are in excellent agreement with field data (Fig. 13 of Ewans 1998).

Bimodal directional distribution has been observed from spatial measurements using an aerial stereo photographic technique (Phillips 1958; Cote et al. 1960; Holthuijsen 1983), airborne radar system (Jackson et al. 1985), and land-based imaging radar (Wyatt 1995). In contrast to the analysis of temporal measurements from wave gauge arrays or directional buoys, a standard two-dimensional fast Fourier transformation procedure is sufficient to bring out the multimodal feature in the directional distribution from 3D spatial topographic images. Data quality of earlier stereophotography, however, was not very high. Holthuijsen (1983, p. 192) estimates the dynamic range in their spectral results to be approximately 10 dB. Their data are also significantly affected by the presence of nontrivial swell. The dynamic range of the spectra presented in Cote et al. (1960) is much higher. Based on the contour plots such as those shown in their Fig. 10.12, it is judged that the dynamic range of that dataset is close to 20 dB.

Technology has advanced significantly since those wave mapping missions. Specifically, the aircraft motion can be determined more accurately due to the advent of the kinematic GPS (Global Positioning System) technology. As a result, the signal to noise ratio of the measurement also improved considerably. An airborne topographic mapper (ATM: an airborne scanning lidar ranging system) has been deployed recently for mapping surface waves (Hwang et al. 1998). The dynamic range of the present measurements from the airborne lidar is approximately 30 dB, that is, 10 to 100 times improved over the earlier topographic datasets. In Part I (Hwang et al. 2000), the data quality of the ATM measurements is critically examined. The spectral properties in terms of the spectral slope and the dimensionless spectral coefficient are in excellent agreement with existing results based on the analyses of several decades of frequency spectral data. The ATM measurements are also compared with data measured by an offshore buoy deployed in the same region. The agreement is also quite satisfactory. These comparisons have established our confidence in the ATM data. In this paper, we proceed with the data analysis aiming to quantify the wavenumber dependence of the directional distribution from the ocean surface topography obtained by the ATM. The measurement technique and environmental conditions of the field experiment have been described in Part I. A brief summary is given in section 2. In that section, we also present a short discussion on the directional resolution of the 2D spectrum computed form 3D topography. The analysis of the spectral directional distributions is described in section 3. Functional forms of several key parameters of the distribution function (the spreading factor in terms of the moments of the directional distribution and bimodal features in terms of the lobe angle and lobe ratio) are established from the 2D wavenumber spectra. Polynomial fitting to the Fourier components of the distribution functions is performed and the coefficients for the leading nine components are

tabulated. The results are also compared with four established directional distribution models (Mitsuyasu et al. 1975; Hasselmann et al. 1980; Donelan et al. 1985; Banner 1990). We also compare the measured directional distributions with those derived from numerical experiments using a nonlinear wave model (Banner and Young 1994) to investigate the frequency dependence of the dissipation function. Finally, the ATM results are compared with the directional information derived from MEM and MLM processing of buoy data. It is found that although bimodal feature can be extracted from MEM processing, the quantitative results on the integral properties such as the spreading factor, lobe angle, and lobe amplitude are not accurately determined. The root mean square differences between MEM and ATM results are not better than the counterparts between MLM and ATM results. A summary is given is section 4.

2. Measurement technique and directional resolution

The measurement technique and data processing procedure using the ATM have been presented in Hwang et al. (2000, hereafter Part I); a brief summary is presented here. The ATM measures the distance between the aircraft and the surface of the ground or ocean using a scanning laser beam. Designed for Greenland Icecap monitoring as a part of the global warming project (Krabill et al. 1995a,b), the laser beam scans a circular pattern with a fixed incident angle of 15°. Carried on an aircraft, the system achieves the goal of 2D mapping to produce 3D surface topography. The aircraft altitude is typically 500 m and the flight speed is approximately 60 m s^{-1}. The dispersion angle of the laser beam is 1 mrad and the footprint of the laser spot on the ocean surface is 0.5 m. The swath of the image is 250 m. The scanning pattern repetition rate is 10 Hz and the data sample rate is 5000 Hz; therefore, each scanning circle is divided into 500 segments. The coarsest spacing between neighboring image pixels is 1.6 m in the cross-track direction and 6 m in the along-track direction. The circular-scan data are subsequently resampled into rectangular grids referenced to the flight track direction. Through some experimentation, square grids with 3-m grid size are chosen for the data presented here. Because the Nyquist wavenumber, k_{Ny}, is dictated by the coarsest spacing of the original data, the computed spectral components in the range of $k \leq k_{\mathrm{Ny}}$ are emphasized. The data processing procedures have been discussed in Part I. Key spectral properties in terms of the spectral slope and the dimensionless spectral coefficient have been shown to be in good agreement with existing results derived from time series (frequency domain) measurements.

One of the unique features of the 3D topographic data is its exceptional directional resolution in the resulting 2D wavenumber spectrum. With reference to Fig. 1, the area of the ring with a width Δk and radius k is

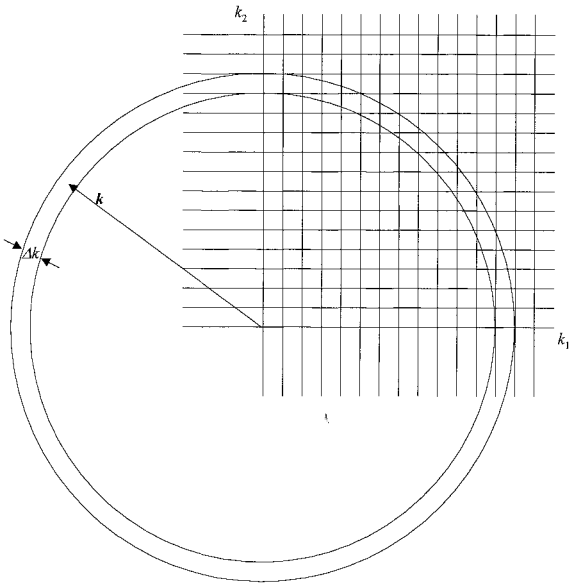

FIG. 1. A sketch illustrating the wavenumber dependence of the directional resolution of the 2D spectrum.

$$A = \int_{-\pi}^{\pi} \int_{k-\Delta k/2}^{k+\Delta k/2} k \, dk \, d\theta = 2\pi k \Delta k. \tag{1}$$

The number of rectangular wavenumber ''pixels'' within the ring is

$$N = \frac{A}{dk_1 dk_2} = \frac{2\pi k \Delta k}{dk_1 dk_2}. \tag{2}$$

The directional resolution is calculated by

$$\Delta\theta = \frac{2\pi}{N} = \frac{dk_1 dk_2}{k\Delta k}. \tag{3}$$

With $\Delta k = dk_1 = dk_2 = k_0$, (3) becomes

$$\Delta\theta = \frac{k_0}{k} \text{ rad} = \frac{57.32^\circ}{k/k_0}. \tag{4}$$

For the data presented in this paper, $k_0 = 2\pi/(128\Delta x) = 0.016$ rad m^{-1} for $\Delta x = 3$ m, and the peak wavenumber $k_p = 0.098$ rad $m^{-1} \approx 6\ k_0$ (Part I). For $k \geq k_p$, the directional resolution is better than 10°. Figure 2 shows a comparison of the measured N and $\Delta\theta$ with the analytical solutions [Eqs. (2) and (4)]; the agreement is very good.

The same results on the directional resolution can be derived from equating the integration ''area elements'' of the rectangular and polar coordinates; that is, $dk_1 dk_2 = k dk d\theta$. With the substitution of $dk_1 = dk_2 = dk = \Delta k = k_0$, $d\theta = k_0/k$ [rad], which is identical to (4).

3. Directional distribution of the wavenumber spectrum

On 24 September 1997, the ATM acquired 4 hours (from 1200 to 1600 UTC) of data near Duck, North

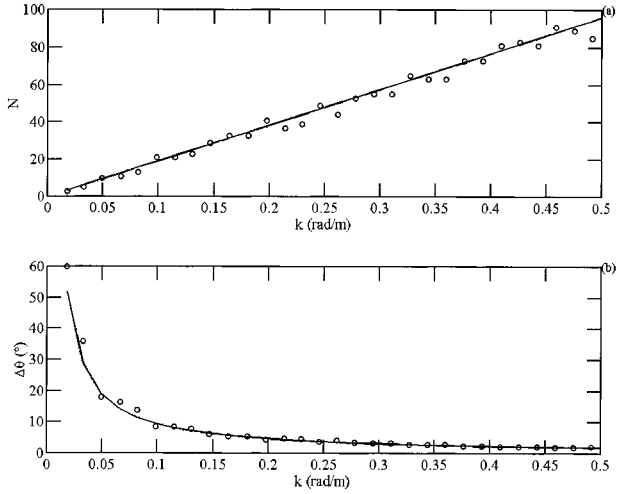

FIG. 2. A comparison of the measured N and $\Delta\theta$ with the analytical solutions, Eqs. (2) and (4), respectively.

Carolina. A front passed through the area the night before. Wind speed increased from 4 to 12 m s^{-1} within a 2-h period (0230–0430 UTC 24 September) and the wind direction shifted from westerly to northerly. Wind speed was quasi-steady at approximately 9.5 m s^{-1} from 0600 to 1300 UTC 24 September, and then decreased from 9.5 m s^{-1} at 1300 UTC to 5.5 m s^{-1} at 1600 UTC. Wave records show that the wave conditions (significant wave height and peak wave period) were quasi-steady during the first 2 hours of the flight. During the last 2 hours, the wave conditions decayed slowly. More information on the environmental conditions and spectral analysis procedures are given in Part I.

An example of the resulting 2D wavenumber spectrum, presented as $\Psi(k_1, k_2)$, $\Psi(k, \theta)$, and $\Psi(\omega, \theta)$, is shown in Fig. 6 of Part I. (This figure is reproduced as Fig. 3 here.) It is observed that the directional distribution is generally symmetric with respect to the dominant wave direction (the wavenumber vector $k = 0.098$ rad m^{-1}, $\theta = 45°$ is plotted in Fig. 3a). The peak wave-

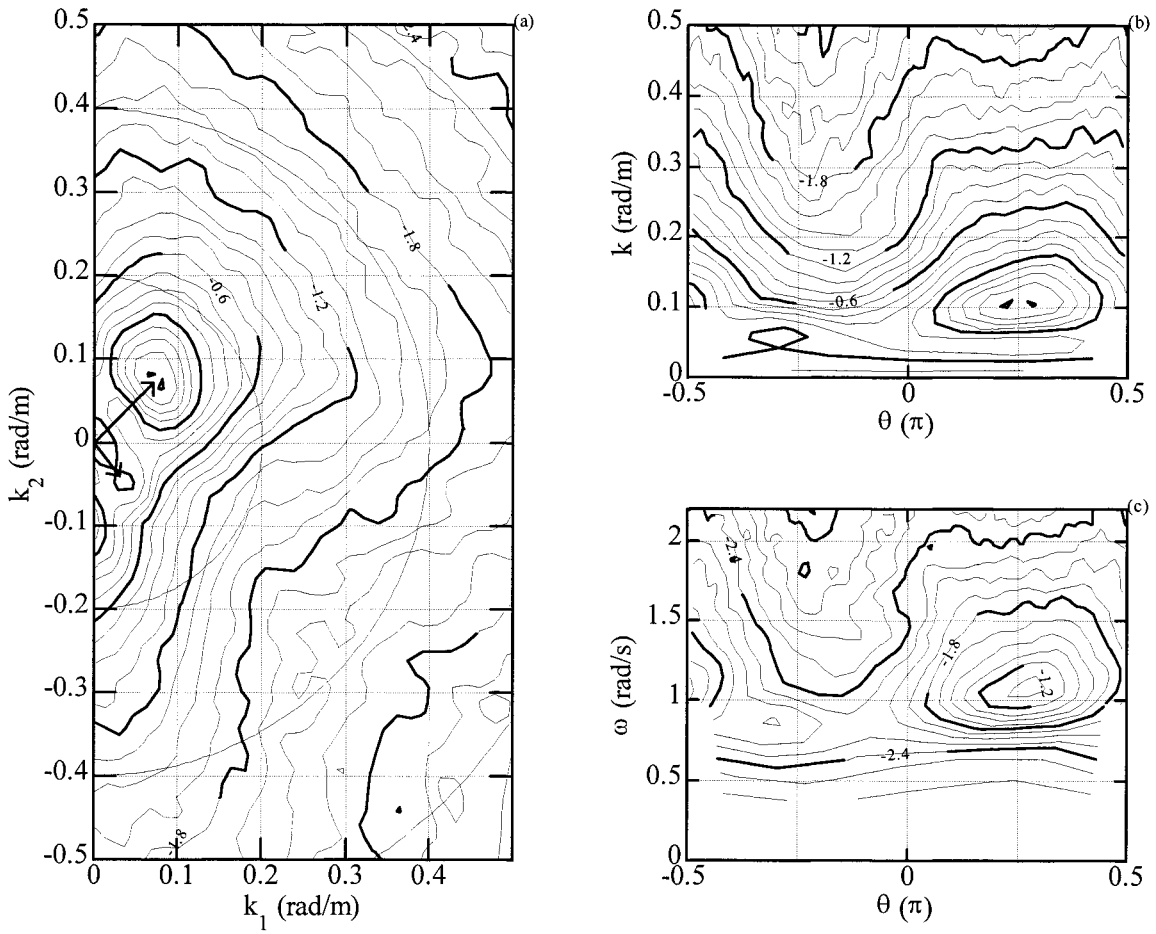

FIG. 3. Examples of the computed 2D wavenumber spectra. (a) Contour plot in (k_1, k_2) representation (same as polar representation). Wavenumber vectors for the dominant wind wave and the swell components are indicated by arrows. (b) Contour plot in orthogonal (k, θ) representation. (c) Contour plot in orthogonal (ω, θ) representation. Semicircles in (a) correspond to $k = 0.2$, 0.4, and 0.6 rad m^{-1}. The intervals are 6 dB apart (i.e., 0.6 in logarithmic scale) for the thick contours, and 1.5 dB apart for the thin contours. [Reproduced from Fig. 5 in Hwang et al. (2000).]

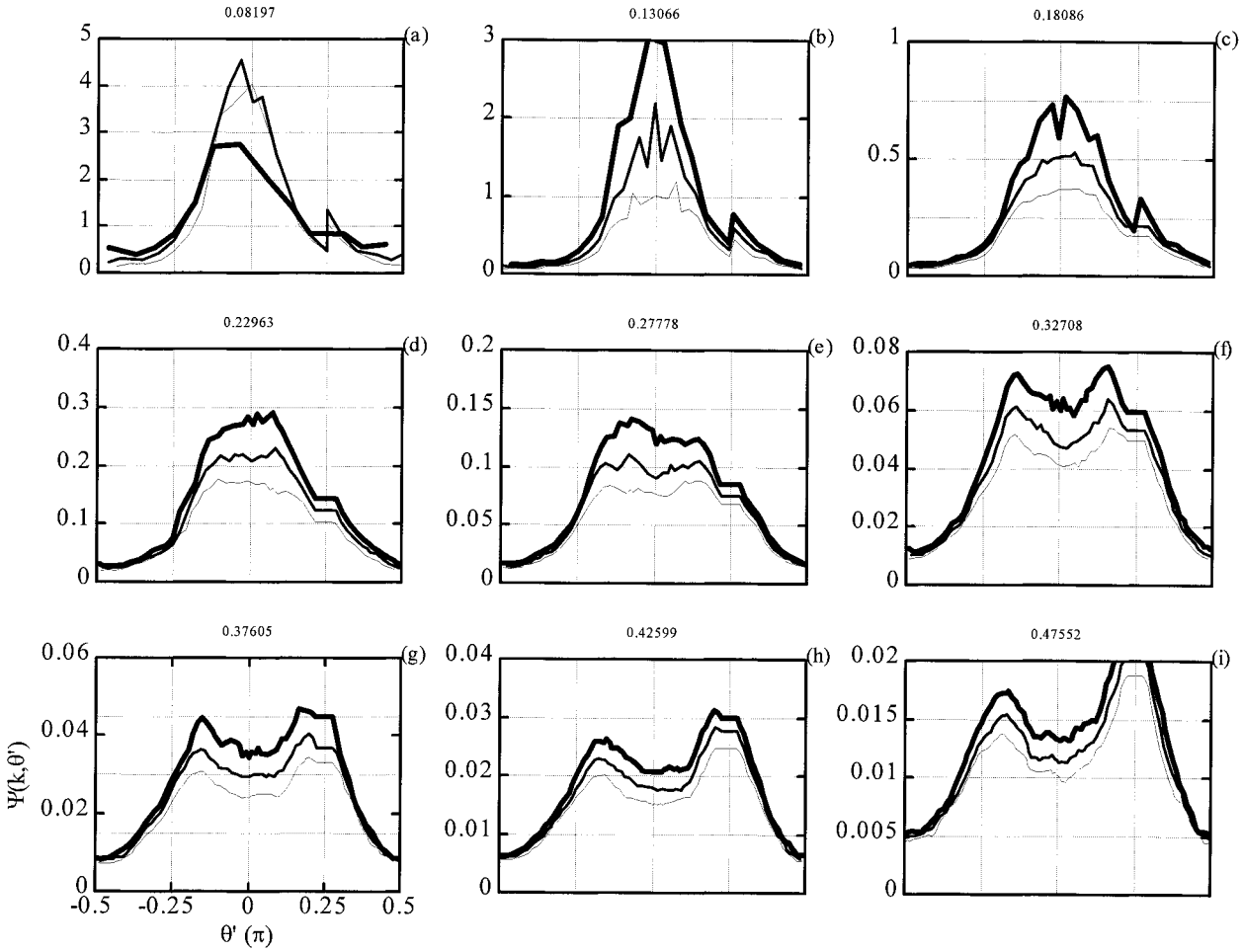

FIG. 4. Directional distributions of the spectral intensities at 27 discreet wavenumber components. Three distributions are plotted in each panel (a)–(i). The wavenumber spacing of the distributions is $k_0 = 0.0164$ rad m^{-1} ($k_0 = 2\pi/128\Delta x$, where $\Delta x = 3$ m). The starting wavenumber for the three curves in each panel is printed at the top of the panel. The line thickness decreases with increasing wavenumber in each panel.

number, $k_p = 0.098$ rad m^{-1}, is determined from the integrated omnidirectional spectrum (see Part I). The 2D spectrum displayed in Fig. 3 shows that the directional spreading becomes broader as wavenumber increases. Bimodal distribution starts to develop for wavenumber slightly greater than $\sim 2k_p$. The angular separation of the distribution lobes increases toward higher wavenumber or wave frequency. More quantitative analysis of the directional distribution is presented below. For a reference of the data processing coordinates and the geographic orientations, Fig. 1 of Part I displays the flight tracks superimposed on the map of the experimental site and a sketch showing relevant directions.

a. Fourier decomposition

Significant variations in the directional distribution in different wavenumber ranges can be deduced from inspecting the 2D wavenumber spectra such as those shown in Fig. 3. Most interesting of all, it is noticed that a unimodal distribution occurs only in a narrow wavenumber range near the spectral peak, $k_p = 0.098$ rad m^{-1}. Outside of this small range, the directional distribution becomes more uniform and a bimodal distribution becomes prominent. The spacing of the two lobes increases as wavenumber increases. To illustrate the evolution of the directional distribution with wavenumber, $\Psi(k, \theta)$ versus θ for 27 wavenumbers are plotted in Figs. 4a–i. In each panel of the figure, three distributions are displayed. The line widths of the three curves decrease with increasing wavenumber. The wavenumber spacing k_0 is 0.0164 rad m^{-1} ($k_0 = 2\pi/128\Delta x$ where $\Delta x = 3$ m; see Part I for details of the spectral processing procedure). The starting wavenumber for the three curves in each panel is printed at the top of the panel. The direction shown is shifted by $-45°$ to align with the dominant wave direction. The new direction is denoted by θ' ($\theta' = \theta - \theta_p$). [Note that the angular range of $\pi/2 \geq \theta' \geq \pi/4$ corresponds to the original direction range of $3\pi/4 \geq \theta \geq \pi/2$, which

is in the ''discarded half-plane'' of the 2D spectrum (due to a 180° ambiguity of the 2D spectrum from plane image; see Fig. 3a).] For display purposes, the data within the original range of $-\pi/2 \geq \theta \geq -\pi/4$ are shifted into this range, which explains the apparent discontinuity at $\theta' = \pi/4$. As shown in section 2, the directional resolution is dependent on wavenumber because the number of ''pixels'' in the (k_1, k_2) space increases linearly with k (Fig. 2b). The results shown in Fig. 4 have the directional resolution degraded to 10° uniformly for $k > k_p$. In general the directional distribution function is reasonably symmetric. Because data in the region near $\theta' = \pi/4$ ($\theta = \pi/2$) may be affected by the 180° spectral ambiguity typically occurring in the processing of still images, for Fourier decomposition analysis, $\Psi(k, \theta')$ in the range $-\pi/2 \geq \theta' \geq 0$ is mirrored to the range $\pi/2 \geq \theta' \geq 0$. The distribution function for each wavenumber is then linearly interpolated to 32 equally spaced angular bins and its Fourier components computed.

Extensive discussions of the analysis method have been presented in earlier publications (e.g., Cote et al. 1960; Longuet-Higgins et al. 1963). From this point on, the prime in θ' will be dropped and all references to the direction are with respect to the dominant wave direction. The directional spectrum can be written in the form

$$\Psi(k, \theta) = k^{-1}\chi(k)D(k, \theta), \tag{5}$$

with $D(k, \theta) \geq 0$ and

$$\int_{-\pi/2}^{\pi/2} D(k, \theta)\, d\theta = 1. \tag{6}$$

The integration limits in (6) are from $-\pi/2$ to $\pi/2$. As discussed in Cote et al. (1960), the Fourier decomposition of such a directional distribution function is given by

$$D(k, \theta) = \frac{1}{\pi}\left[1 + \sum_{n=1}^{N} A_n(k)\cos 2n\theta + B_n(k)\sin 2n\theta\right], \quad -\pi/2 \leq \theta \leq \pi/2. \tag{7}$$

If the distribution function is symmetric with respect to θ, the odd function terms $[B_n \sin(2n\theta)]$ vanish and the distribution function is fully represented by

$$D(k, \theta) = \frac{1}{\pi}\left[1 + \sum_{n=1}^{N} A_n(k)\cos 2n\theta\right], \quad -\pi/2 \leq \theta \leq \pi/2. \tag{8}$$

Alternatively, the direction distribution can be extended to the full range of $-\pi$ to π, by extrapolation, for example. Denoting the extrapolated directional distribution as $D_2(k, \theta)$, the corresponding Fourier decomposition is

$$D_2(k, \theta) = \frac{1}{2\pi}\left[1 + \sum_{n=1}^{N} a_n(k)\cos n\theta + b_n(k)\sin n\theta\right], \quad -\pi \leq \theta \leq \pi. \tag{9}$$

Again, for a symmetric function, b_n terms vanish:

$$D_2(k, \theta) = \frac{1}{2\pi}\left[1 + \sum_{n=1}^{N} a_n(k)\cos n\theta\right], \quad -\pi \leq \theta \leq \pi. \tag{10}$$

In practice, (8) converges much faster than (10) and requires significantly less number of terms to represent the directional distribution. The price paid is that the data in the range of $|\theta| > \pi/2$ are discarded. In the case of the analysis of 2D wavenumber spectra from 3D topographic data, this is not a loss as the directional information in the range $|\theta| > \pi/2$ is not available in the first place. Figure 5 compares the two different decompositions of the function

$$D(\theta) = \cos^{20}\frac{\theta}{2}, \qquad -\pi \leq \theta \leq \pi. \tag{11}$$

The Fourier coefficients A_n (circles) and a_n (pluses) are shown in Fig. 5a. The comparison of the original waveform (11) with the Fourier summations computed by (8) and (10) are shown in Figs. 5b and 5c, respectively. In both panels, circles represent the original waveform (11), solid curves represent summations with $N = 2$ and dotted curves are for $N =$ maximal number of decomposed components, 16 for Figs. 5b and 32 for Fig. 5c. The typical output from directional buoys is the first two terms of the Fourier series in (10); thus the solid curves represent a realistic approximation from buoy measurements. The more speedy convergence using (8) is clearly illustrated from these comparisons; the curves for $N = 2$ and 16 are essentially identical in Fig. 5b. In contrast, the two-term solution using (10) is a poor representation of the original waveform (Fig. 5c) and the directional spreading of the resulting approximation is much wider than the original waveform. We also computed the variance fractions of 2-, 3-, 4-, and 6-term summations using (8) and (10) for the function $\cos^p(\theta/2)$ with p varying from 1 to 40. The variance fraction as a function of p is shown in Fig. 5d. In all cases, the two-term summations using (8) produce better result than four-term summations using (10). Also, using (8), the four-term summation recovers almost the total variance, even for a very narrow directional distribution close to $\cos^{40}(\theta/2)$.

The wavenumber dependence of the first four Fourier coefficients of the measured directional distributions computed with (8) is illustrated in Fig. 6. The spectrum is obtained from averaging the first half (2 h) of the experiment when the wave condition was quasi-steady. Separate computation is performed for the second half when the wave field was decaying (Part 1). Little difference in the directional distributions is found between

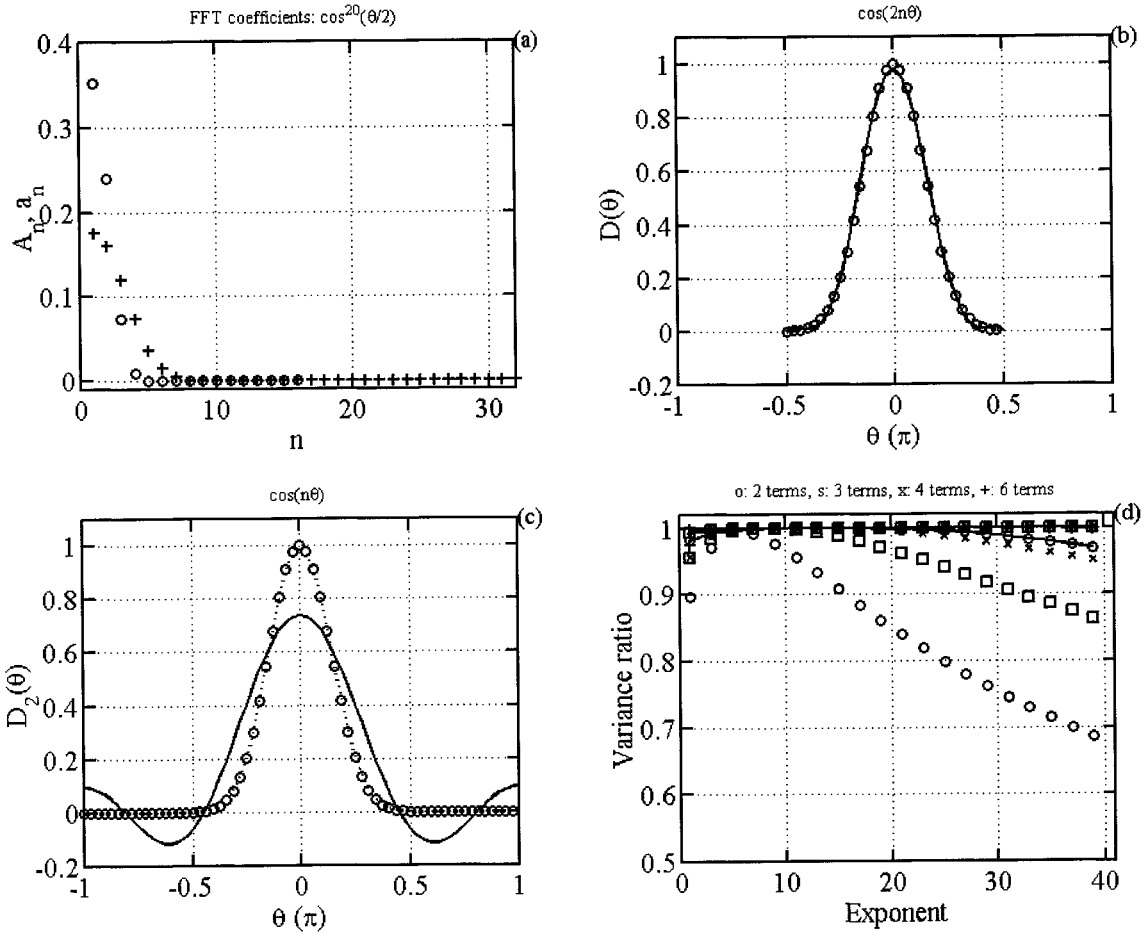

FIG. 5. A comparison of two Fourier decompositions [Eqs. (8) and (10)] of the function specified by (11). (a) The spectral coefficients are circles: calculated by (8) and pluses: calculated by (10). (b) Comparison of the original data (circles) with 2-term (solid curve) and 16-term (dotted curve) summations using (8). (c) Comparison of the original data (circles) with 2-term (crosses) and 32-term (pluses) summations using (10). (d) Variance fractions of 2-term (circles), 3-term (squares), 4-term (crosses), and 6-term (pluses) summations of the Fourier components. Connected symbols are computed by (8) and symbols only are computed by (10).

the spectra from the two half-periods. The coefficients of the third-order polynomial fitting to the leading nine Fourier coefficients for both quasi-steady and decaying wave fields are given in Table 1.

The directional distributions reconstructed using the Fourier components regenerated by the polynomial coefficients (Table 1) are plotted in Fig. 7. The distribution functions are normalized such that the magnitude at the dominant wave direction is unity. Other normalization schemes can also be used and will be discussed in the next section. Results using two, four, six, and eight Fourier components are illustrated in panels a, b, c, and d, respectively. Development of the bimodal feature as k/k_p increases can be reproduced with as little as two Fourier components but four Fourier components are needed to give sufficient representation of the lobe amplitude and to avoid negative values in the directional distribution. The directional distribution constructed with four Fourier components will be denoted as $D_{k,\mathrm{FFT4}}(\theta)$ in subsequent discussions.

b. Global properties

Here we present a few global properties of the directional distribution as analyzed using the 3D surface topography. The integration of the directional distribution function is calculated by

$$I_D(k) = \int_{-\pi/2}^{\pi/2} D_k(\theta)\, d\theta, \tag{12}$$

where $I_D(k)$ and $D_k(\theta)$ are related by

$$D(k, \theta) = \frac{D_k(\theta)}{I_D(\theta)} \tag{13}$$

to assure that (6) is satisfied. Two normalization meth-

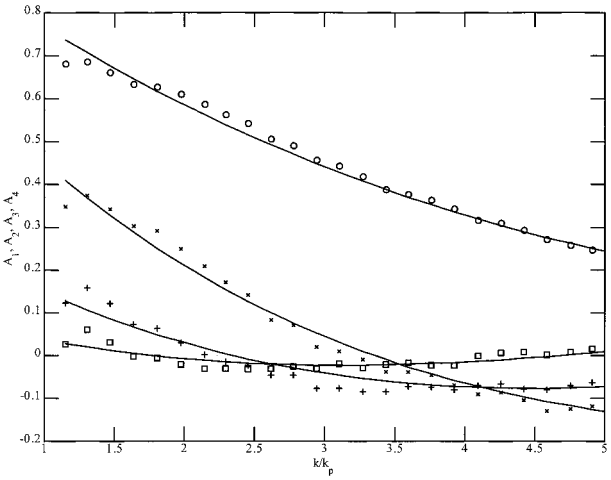

FIG. 6. The (normalized) wavenumber dependence of the first four Fourier components of the directional distributions. Symbols are circles, crosses, pluses, and squares for the first to the fourth components, respectively, Curves are third-order polynomial fitted. The coefficients of fitting for the leading nine Fourier coefficients are listed in Table 1.

ods are applied. The first method obtains $D_k(\theta)$ from normalizing $\Psi(k, \theta)$ by the maximum value of the array; that is,

$$D_{k,1}(\theta) = \frac{\Psi(k, \theta)}{\max[\Psi(k, \theta)]}. \tag{14}$$

The integration is denoted as $I_{D,1}(k)$. This is one of the most common ways of displaying the directional distribution. The results of $I_{D,1}(k)$ are shown in Fig. 8a, and can be approximated by the following function

$$I_{D,1}\left(\frac{k}{k_p}\right) = \begin{cases} 0.85\left(\dfrac{k}{1.3k_p}\right)^{-1}, & \dfrac{k}{k_p} < 1.3 \\ 0.85\left(\dfrac{k}{1.3k_p}\right)^{0.8}, & 1.3 \le \dfrac{k}{k_p} < 5 \\ 2.5, & \dfrac{k}{k_p} \ge 5. \end{cases} \tag{15}$$

These results show that the smallest directional spreading occurs at $1.3k_p$, denoted as k_n in the following discussions. Equation (15) is plotted as the solid curve in Fig. 8a. Interestingly, the rate of increase of the measured $I_{D,1}(k)$ versus k/k_p decreases and appears to approach an asymptotic value between 2.4 and 2.8 (Fig. 8a). The asymptotic value is very close to $I(0.5) = \int_{-\pi/2}^{\pi/2} \cos^{0.5}\theta \, d\theta$ (Part I), which is 2.3963. Through dynamic and statistical arguments, Phillips (1985) has reached the conclusion that the integrated directional distribution of gravity waves in the equilibrium range is best represented by $I(0.5)$. The data shown in Fig. 8a provide direct support for Phillips' conclusion.

The integration of the directional distribution function is closely related to the spreading function. For example, $I_{D,1}(k)$ is related to the spreading parameter b in the sech squared ($\mathrm{sech}^2 b\theta$) directional distribution function suggested by Donelan et al. (1985), $b(k) = 2/I_{D,1}(k)$. The results reported in Donelan et al. [1985, Eq. (8.4)] are plotted as a dashed curve in Fig. 8a. The curve is shifted toward low wavenumber because their results show that the narrowest spreading occurs at $k_m = 0.90k_p$ ($\omega_n = 0.95\ \omega_p$). Also, in the data of Donelan et al. (1985), the calculated b in the high-frequency region ($\omega > 1.6\omega_p$) appears to be rather noisy, which created the artificial

TABLE 1. Third-order polynomial fitting ($y = c_1x^3 + c_2x^2c_3x + c_4$, where y is $A_1, A_2, \ldots, A_9$, and x is k/k_p) of the Fourier coefficients of the directional distribution.

	c_1	c_2	c_3	c_4
		(a) Quasi-steady wave field		
A_1	-6.83×10^{-4}	2.20×10^{-2}	-2.42×10^{-1}	9.87×10^{-1}
A_2	-2.66×10^{-3}	5.32×10^{-2}	-3.82×10^{-1}	7.83×10^{-1}
A_3	-1.44×10^{-3}	3.29×10^{-2}	-2.08×10^{-1}	3.26×10^{-1}
A_4	-1.13×10^{-3}	2.15×10^{-2}	-1.01×10^{-1}	1.17×10^{-1}
A_5	-7.22×10^{-4}	1.09×10^{-2}	-4.70×10^{-2}	5.96×10^{-2}
A_6	-9.04×10^{-4}	1.21×10^{-2}	-4.92×10^{-2}	7.40×10^{-2}
A_7	5.92×10^{-4}	-8.34×10^{-3}	2.75×10^{-2}	-9.78×10^{-3}
A_8	-1.10×10^{-3}	1.57×10^{-2}	-7.13×10^{-2}	9.80×10^{-2}
A_9	4.33×10^{-4}	-5.93×10^{-3}	2.06×10^{-2}	-1.52×10^{-2}
		(b) Decaying wave field		
A_1	-6.83×10^{-4}	2.09×10^{-2}	-2.42×10^{-1}	9.69×10^{-1}
A_2	-3.57×10^{-3}	6.99×10^{-2}	-4.49×10^{-1}	8.17×10^{-1}
A_3	-2.78×10^{-3}	4.91×10^{-2}	-2.55×10^{-1}	3.39×10^{-1}
A_4	-6.52×10^{-4}	1.20×10^{-2}	-5.09×10^{-2}	3.08×10^{-2}
A_5	8.30×10^{-4}	-1.38×10^{-2}	7.02×10^{-2}	-1.00×10^{-1}
A_6	-7.68×10^{-4}	9.12×10^{-3}	-3.13×10^{-2}	3.94×10^{-2}
A_7	1.33×10^{-4}	-1.89×10^{-3}	4.18×10^{-3}	5.97×10^{-3}
A_8	6.82×10^{-4}	-9.91×10^{-3}	3.86×10^{-2}	-3.58×10^{-2}
A_9	-2.50×10^{-5}	4.58×10^{-4}	-2.70×10^{-3}	1.83×10^{-3}

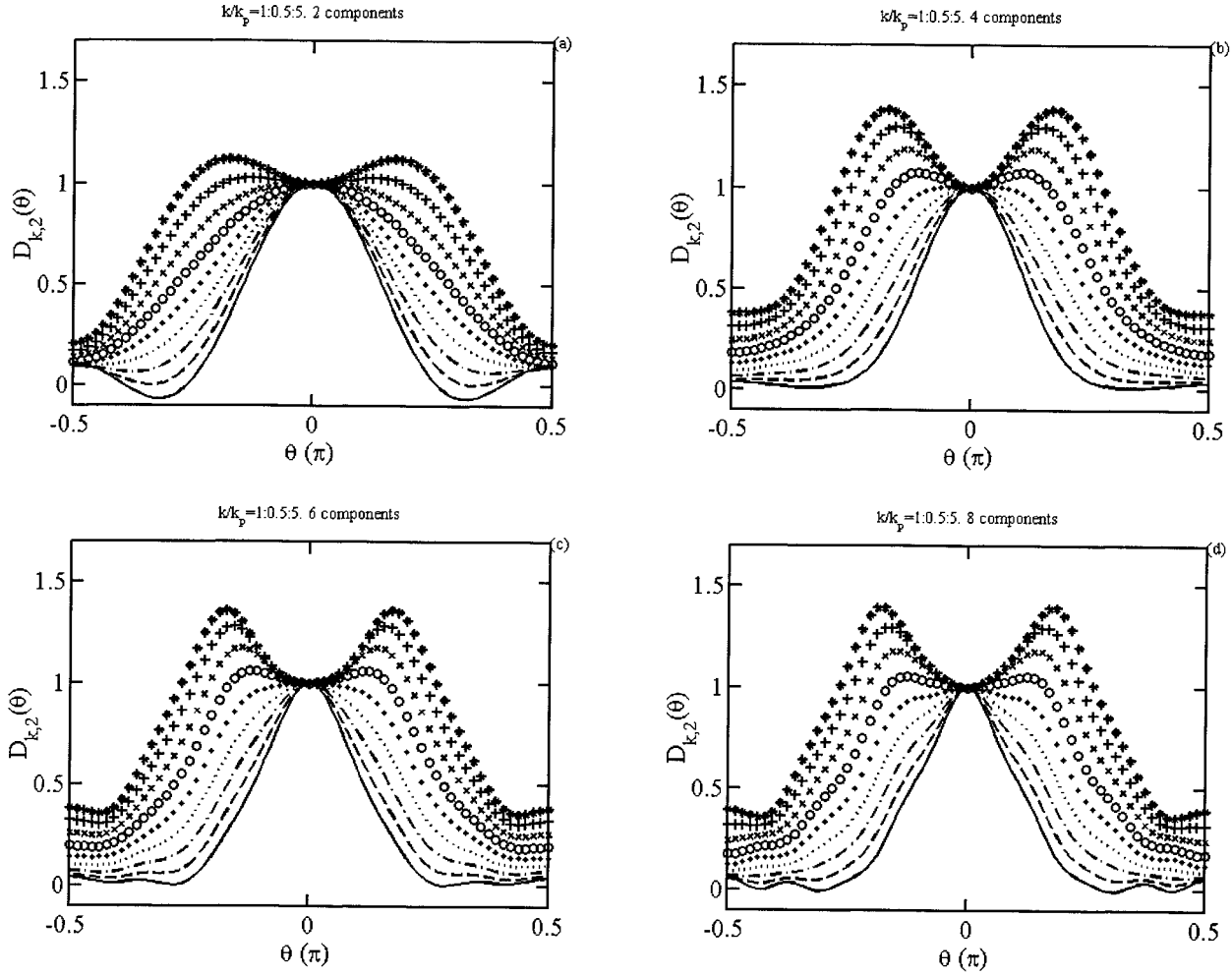

FIG. 7. The directional distributions computed with Fourier coefficients generated by the polynomial fitting coefficients (Table 1). (a) Two-component summations, (b) four-component summations, (c) six-component summations, and (d) eight-component summations. The dimensionless wavenumber k/k_p varies from 1 to 5 in steps of 0.5 rad m^{-1} for the sequence of curves represented by solid, dashed, dashed–dotted, dotted, dots, circles, crosses, pluses, and asterisks.

flattening of their curve (dashed line) for the region $k/k_p \geq 2.56$. Banner (1990) revised the b values in the high wavenumber region and proposed a modified direction model [Eq. (2.9) of Banner (1990)] which is plotted as dashed-and-dotted curve in the figure. The modified model is in excellent agreement with the present data in the wavenumber range $k > \sim 3k_p$.

The directional distribution can also be normalized by the spectral value at the dominant wave direction; that is,

$$D_{k,2}(\theta) = \frac{\Psi(k, \theta)}{\Psi(k, \theta_p)}. \tag{16}$$

This representation is more convenient for the construction of bimodal distribution models, such as the double Gaussian distribution proposed by Ewans (1998), or for describing the generation of directional wave components from a nonlinear wave–wave interaction mechanism, such as the numerical experiments described in Banner and Young (1994). The integration will be denoted as $I_{D,2}(k)$. The results are shown in Fig. 8b. The data can be approximated by two branches

$$I_{D,2}\left(\frac{k}{k_p}\right) = \begin{cases} 0.91\left(\dfrac{k}{1.3k_p}\right)^{-1}, & \dfrac{k}{k_p} < 1.3 \\ 0.91\left(\dfrac{k}{1.3k_p}\right), & 1.3 \leq \dfrac{k}{k_p} < 5. \end{cases} \tag{17}$$

The directional spreading factor can be quantified by the moment of the directional distribution,

$$\theta_{b,m}(k) = \left[\frac{\displaystyle\int_0^{\pi/2} \theta^m D_k(\theta)\, d\theta}{\displaystyle\int_0^{\pi/2} D_k(\theta)\, d\theta}\right]^{1/m}, \qquad m = 1, 2, \cdots. \tag{18}$$

The first two moments are shown in Fig. 9. Computed

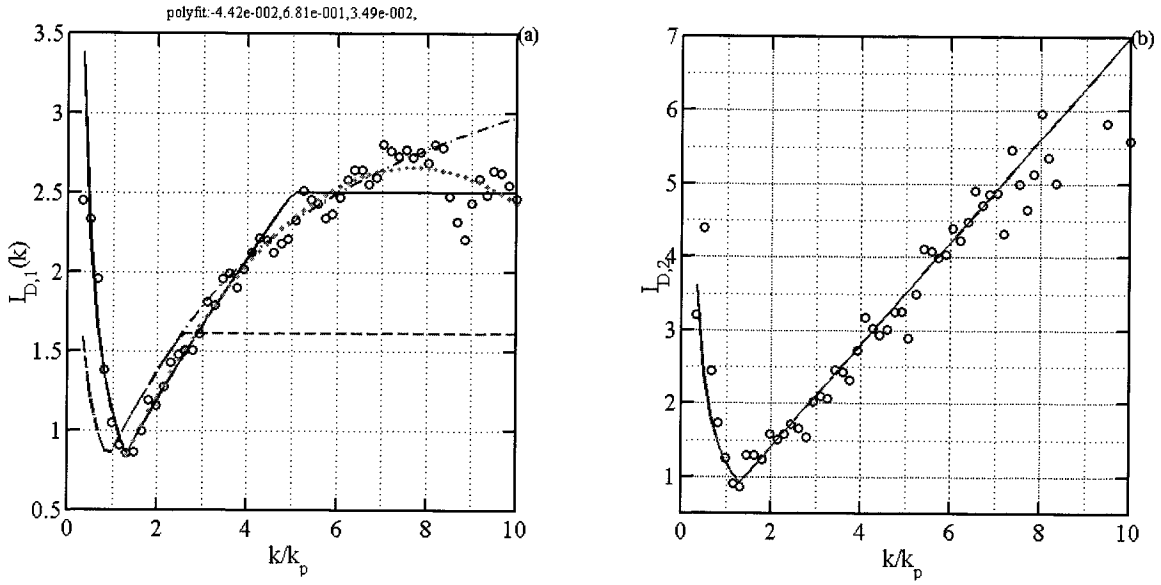

FIG. 8. The integrated directional distribution $I_{D,1}$ (a) From solid curve: Eq. (15), dashed curve: Donelan et al. (1985), dashed–dotted curve: Banner (1990), and $I_{D,2}$ (b) From solid curve: Eq. (17).

results based on the directional distribution functions of Mitsuyasu et al. (1975), Hasselmann et al. (1980), and Donelan et al. (1985) for the present C_p/U_{10} condition are also superimposed on Figs. 10a and 10b as dashed, dashed–dotted, and solid curves, respectively. The directional distribution functions of Mitsuyasu et al. (1975) and Hasselmann et al. (1980) are of the cos squared form $[\cos^{2s}(\theta/2)]$, with s expressed as functions of wave age, C_p/U_{10}. Donelan et al. (1985) and Banner (1990) use a sech squared function $[\mathrm{sech}^2(b\theta)]$. Detailed comparisons of these four distribution functions have been presented in Young (1994) and Ewans (1998) and will not be repeated here. In the region close to the spectral peak, the calculated spreading factor is smallest (narrowest beamwidth) using the Donelan et al. (1985) formulation, and followed in sequence by Mitsuyasu et al. (1975) and Hasselmann et al. (1980). The exponents $2s$ of the cos squared distribution models of Mitsuyasu et al. (1975) and Hasselmann et al. (1980) are 25 and 14, respectively, at the spectral peak. The b value of the sech squared model of Donelan et al. (1985) is 2.28 at the spectral peak, and $\mathrm{sech}^2(2.28\theta)$ is very close to $\cos^{40}(\theta/2)$. In the long-wave region ($k/k_p < 1$), the increase of spreading toward low wavenumber is steeper than for the three directional models. In the region $k > k_p$, most of the measured data fall below the model prediction. The apparent broader spreading of the model prediction is expected since those models are constructed based on measurements from sensor systems that provide either two or three Fourier components of the distribution function using Fourier expansion (10). As illustrated in Fig. 5c and 5d, the two- and three-term Fourier approximations using (10) produce only mediocre agreement with the true waveform.

The coefficients of the polynomial fitting to the measured directional moments are listed in Table 2. Two sets of fittings are performed for the quasi-steady and decaying wave conditions (Tables 2a and 2b). For each set, the data in the ranges of $0.5 < k/k_p < 1.3$ and $1.3 \le k/k_p < 5$ are listed separately. The fitted curves are plotted as solid lines in Figs. 10c and 10d. The distributions moments (in radian) can also be approximately by two linear segments (shown as dashed–dotted curves in Figs. 10c and 10d),

$$\theta_{b,1}\left(\frac{k}{k_p}\right) = \begin{cases} 0.35 + 1.05\left(1 - \dfrac{k}{k_p}\right), & \dfrac{k}{k_p} < 1.05 \\ 0.30 + 0.087\left(\dfrac{k}{k_p} - 1\right), & 1.05 \le \dfrac{k}{k_p} < 5, \end{cases} \tag{19a}$$

and

$$\theta_{b,2}\left(\frac{k}{k_p}\right) = \begin{cases} 0.52 + 1.05\left(1 - \dfrac{k}{k_p}\right), & \dfrac{k}{k_p} < 1.05 \\ 0.47 + 0.079\left(\dfrac{k}{k_p} - 1\right), & 1.05 \le \dfrac{k}{k_p} < 5. \end{cases} \tag{19b}$$

Computations using the polynomial fitting of four Fourier components $[D_{k,\mathrm{FFT4}}(\theta)]$ are shown as dashed curves (this is done only for data in the higher wavenumber range, $k/k_p > 1$). The four-component solution for the directional distribution yields excellent representation of the measured spreading factor expressed in terms of the moments of the directional distribution.

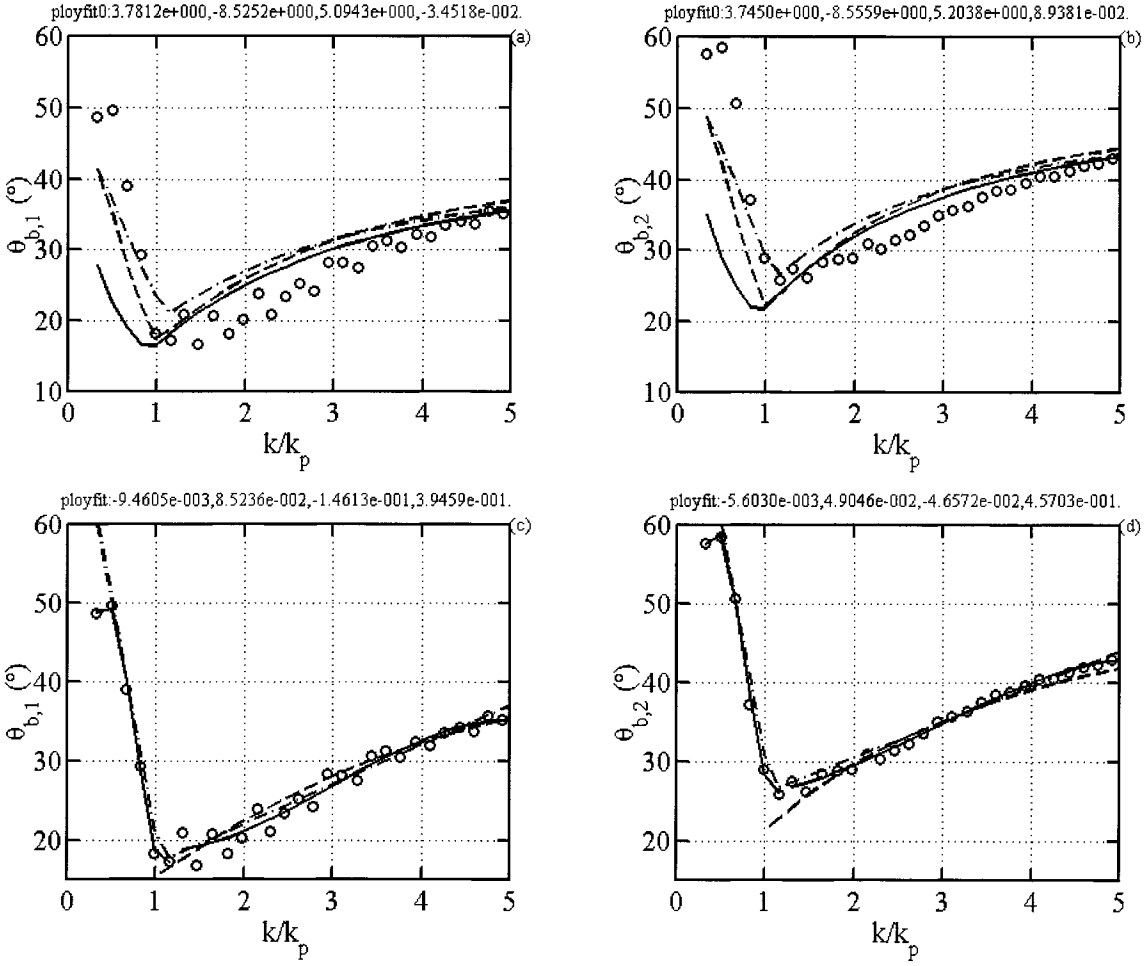

FIG. 9. Directional spreading represented by (a, c) the first moment, and (b, d) the second moment, of $D(k, \theta)$. In (a) and (b), solid curves: Donelan et al. (1985) and Banner (1990), dashed curves: Mitsuyasu et al. (1975), dashed–dotted curves: Hasselmann et al. (1980); in (c) and (d), solid curves: from polynomial fitting (coefficients listed in Table 2), dashed curves: computed by $D_{k,\mathrm{FFT4}}(\theta)$, dashed-and-dotted curve: computed by Eqs. (19a) and (19b), respectively.

c. Bimodal properties

Although the integrated properties of distribution functions calculated from sech squared or cos squared functions (Mitsuyasu et al. 1975; Hasselmann et al. 1980; Donelan et al. 1985) are in reasonably good agreement with measurements, these functions are unimodal and do not represent the true directional distributions such as those shown in Fig. 4. The most distinctive feature of these directional distributions is the bimodal structure, which can be characterized by the locations of the two lobes and the lobe amplitudes. Assuming symmetric distribution with respect to the dominant wave direction, the lobe angle, θ_{lobe}, can be determined by the angular location of the maximal $D_k(\theta)$ using the data in the range $-\pi/2 \leq \theta \leq 0$. The results of the quasi-steady wave field are plotted as a function of k/k_p in Fig. 10a. The coefficients of polynomial fitting to the measured data, divided into two groups of $k/k_p > 1.5$ and $k/k_p < 1.3$, are listed in Table 2, and the fitted curves are plotted as solid curves in the figure. The corresponding results derived from $D_{k,\mathrm{FFT4}}(\theta)$ are plotted as dashed curves. The agreement between measurements and the Fourier approximation is very good.

The sidelobe amplitude can be expressed by the ratio of the maximal $D_k(\theta)$ to its value at the dominant wave direction, $D_k(\theta_p)$. The ratio is termed lobe ratio, r_{lobe}, by Banner and Young (1994), and is shown in Fig. 10b. The coefficients of polynomial fitting are listed in Table 2 and the fitted curves are plotted as solid curves in the figure. The corresponding results calculated with $D_{k,\mathrm{FFT4}}(\theta)$ are shown as dashed curves. The approximation by four Fourier components is in very good agreement with data.

The directional resolution of the distribution data used in Figs. 11a and 11b have been degraded to have uniform directional resolution (32 bins between $-\pi/2$ to $\pi/2$) for different wavenumbers, as done for the Fourier decomposition. This explains the stepwise appearance

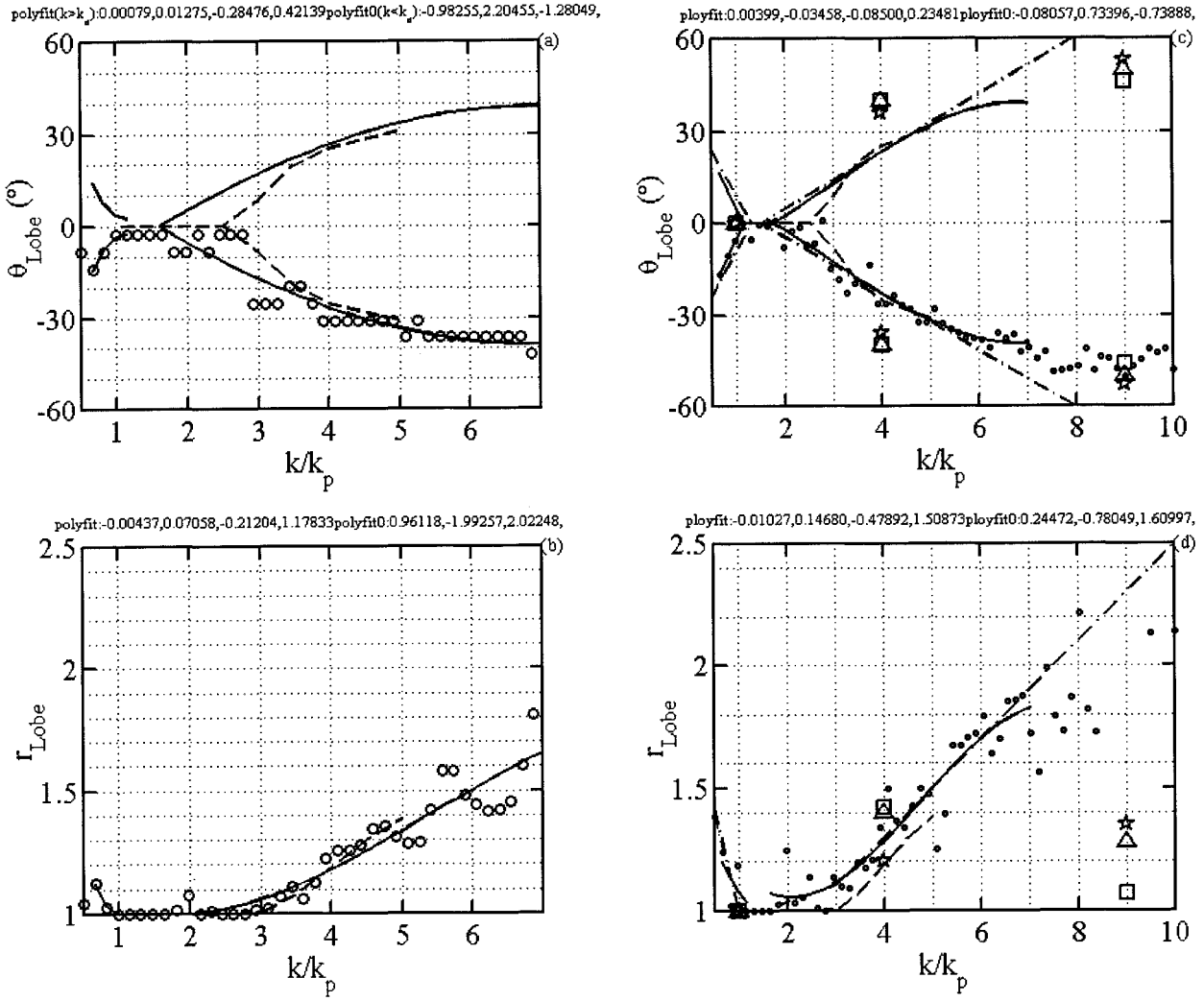

FIG. 10. The lobe angle (a, c) and the lobe ratio (b, d) of the bimodal distribution. In (a) and (b), the directional resolution is degraded to have a uniform resolution as done for the Fourier decomposition procedure. Solid curves: from polynomial fitting (coefficients listed in Table 2), and dashed curves: computed by $D_{k,\mathrm{FFT4}}(\theta)$. In (c) and (d), the directional resolution is not degraded. The dashed-and-dotted curves are computed from Eqs. (20) and (21). Numerical results of Banner and Young (1994) on the effect of dissipation functions are shown with stars: quadratic, triangles: cubic, and square: quartic frequency dependence. Quasi-steady wave field.

of θ_{lobe} in Fig. 10a. Using the original directional distribution data without degrading, the results of θ_{lobe} and r_{lobe} are plotted in Figs. 11c and 11d, respectively. The polynomial fitting coefficients are tabulated in Table 2. The data can also be approximated by linear segments (shown as dashed–dotted curves in the figure). For the lobe angle,

$$\theta_{\mathrm{lobe}}\left(\frac{k}{k_p}\right) = \pm\begin{cases} 150\left(1-\dfrac{k}{k_p}\right), & \dfrac{k}{k_p} < 1 \\ 0, & 1 \le \dfrac{k}{k_p} < 1.5 \\ 9.3\left(\dfrac{k}{k_p}-1\right), & 1.05 \le \dfrac{k}{k_p} < 5. \end{cases} \tag{20}$$

For the lobe ratio,

$$r_{\mathrm{lobe}}\left(\frac{k}{k_p}\right) = \begin{cases} 1 + 0.8\left(1-\dfrac{k}{k_p}\right), & \dfrac{k}{k_p} < 1 \\ 1, & 1 \le \dfrac{k}{k_p} < 1.5 \\ 1 + 0.07\left(\dfrac{k}{k_p}-1.5\right), & 1.5 \le \dfrac{k}{k_p} < 3 \\ 1.1 + 0.2\left(\dfrac{k}{k_p}-3\right), & 3 \le \dfrac{k}{k_p} < 5. \end{cases} \tag{21}$$

The lobe angle and the lobe ratio of the decaying wave field are shown in Fig. 11. Comparing Figs. 10 and 11, it is found that the wavenumber dependencies

TABLE 2. Polynomial fitting ($y = c_1x^3 + c_2x^2 + c_3x + c_4$, where y is the quantities listed in the first column, and x is k/k_p) of the directional parameters ($\theta_{b,1}$, $\theta_{b,2}$, θ_{lobe} and r_{lobe}).

	c_1	c_2	c_3	c_4
(a.1) Quasi-steady wave field, lower-wavenumber branch				
Direction moments ($k/k_p < 1.3$)				
$\theta_{b,1}$	3.78×10^{0}	-8.53×10^{0}	5.09×10^{0}	-3.45×10^{-2}
$\theta_{b,2}$	3.75×10^{0}	-8.56×10^{0}	5.20×10^{0}	8.94×10^{-2}
Lobe angle and ratio, directional resolution not degraded ($k/k_p < 1.3$)				
θ_{lobe}	—	-8.06×10^{-2}	7.34×10^{-1}	-7.39×10^{-1}
r_{lobe}	—	2.45×10^{-1}	-7.80×10^{-1}	1.61×10^{0}
Lobe angle and ratio, directional resolution degraded ($\Delta\theta = 5.6°$)				
θ_{lobe}	—	-9.83×10^{-1}	2.20×10^{0}	-1.28×10^{0}
r_{lobe}	—	0.96×10^{0}	-1.99×10^{0}	2.02×10^{0}
(a.2) Quasi-steady wave field, higher-wavenumber branch				
Direction moments ($k/k_p < 1.3$)				
$\theta_{b,1}$	-9.46×10^{-3}	8.52×10^{-2}	-1.46×10^{-1}	3.95×10^{-1}
$\theta_{b,2}$	5.60×10^{-3}	4.90×10^{-2}	-4.66×10^{-2}	4.57×10^{-1}
Lobe angle and ratio, directional resolution not degraded ($k/k_p < 1.65$)				
θ_{lobe}	3.99×10^{-3}	-3.46×10^{-2}	-8.50×10^{-2}	2.35×10^{-1}
r_{lobe}	-1.03×10^{-2}	1.47×10^{-1}	-4.79×10^{-1}	1.51×10^{0}
Lobe angle and ratio, directional resolution degraded ($\Delta\theta = 5.6°$)				
θ_{lobe}	-7.90×10^{-4}	1.27×10^{-2}	-2.85×10^{-1}	4.21×10^{-1}
r_{lobe}	-4.37×10^{-3}	7.06×10^{-2}	-2.12×10^{-1}	1.18×10^{0}
(b.1) Decaying wave field, lower-wavenumber branch				
Direction moments ($k/k_p < 1.3$)				
$\theta_{b,1}$	2.96×10^{0}	-6.55×10^{0}	3.67×10^{0}	2.44×10^{-1}
$\theta_{b,2}$	3.12×10^{0}	-6.99×10^{0}	4.02×10^{0}	3.29×10^{-1}
Lobe angle and ratio, directional resolution not degraded ($k/k_p < 1.3$)				
θ_{lobe}	—	4.33×10^{-1}	-2.57×10^{-1}	0.33×10^{-1}
r_{lobe}	—	1.10×10^{0}	-2.60×10^{0}	2.59×10^{0}
Lobe angle and ratio, directional resolution degraded ($\Delta\theta = 5.6°$)				
θ_{lobe}	—	-1.72×10^{-2}	3.92×10^{-1}	-4.88×10^{-1}
r_{lobe}	—	1.00×10^{0}	-2.21×10^{0}	2.22×10^{0}
(b.2) Decaying wave field, higher-wavenumber branch				
Direction moments ($k/k_p < 1.3$)				
$\theta_{b,1}$	-4.87×10^{-3}	3.79×10^{-2}	9.03×10^{-3}	2.62×10^{-1}
$\theta_{b,2}$	-7.04×10^{-4}	-1.74×10^{-3}	1.22×10^{-1}	3.04×10^{-1}
Lobe angle and ratio, directional resolution not degraded ($k/k_p < 1.5$)				
θ_{lobe}	-2.70×10^{-3}	5.38×10^{-2}	-4.28×10^{-1}	5.74×10^{-1}
r_{lobe}	-3.30×10^{-4}	-2.67×10^{-2}	3.15×10^{-1}	5.74×10^{-1}
Lobe angle and ratio, directional resolution degraded ($\Delta\theta = 5.6°$)				
θ_{lobe}	-9.90×10^{-4}	3.50×10^{-2}	-3.69×10^{-1}	5.09×10^{-1}
r_{lobe}	-1.40×10^{-4}	-1.23×10^{-2}	1.87×10^{-1}	6.94×10^{-1}

of the lobe angle in quasi-steady and decaying wave fields are essentially identical. There are quantitative differences in the lobe ratio of a quasi-steady wave field and a decaying wave field. In the quasi-steady case, the rate of increase of lobe ratio is approximately constant for the range $7 > k/k_p > 2$ (Fig. 10d). For the decaying case, the lobe ratio in the range $4 > k/k_p > 2$ is higher than the corresponding numbers in a quasi-steady condition. In the range $7 > k/k_p > 4$, the trend is opposite, and the rate of increase of the lobe ratio with respect to k/k_p is much less than that of the quasi-steady case. The linear-segment approximation of the lobe ratio for the decaying case is

$$r_{\text{lobe}}\left(\frac{k}{k_p}\right) = \begin{cases} 1 + 0.8\left(1 - \dfrac{k}{k_p}\right), & \dfrac{k}{k_p} < 1 \\ 1, & 1 \le \dfrac{k}{k_p} < 1.5 \\ 1 + 0.16\left(\dfrac{k}{k_p} - 1.5\right), & 1.5 \le \dfrac{k}{k_p} < 3 \\ 1.1 + 0.067\left(\dfrac{k}{k_p} - 3\right), & 3 \le \dfrac{k}{k_p} < 5. \end{cases} \tag{22}$$

TABLE 3. Comparison statistics of ATM and buoy directional distributions.

Parameter	k/k_p range	Root-mean-square difference		
		ATM vs MLM	ATM vs MEM	ATM vs (MEM + MLM)/2
$I_{D,1}$	0.5–1.3	0.67	0.42	0.56
	1.3–3.0	0.19	0.25	0.14
	3.0–4.76	0.17	0.79	0.43
	0.5–4.76	**0.31**	**0.55**	**0.37**
$I_{D,2}$	0.5–1.3	1.73	1.20	1.41
	1.3–3.0	0.19	0.31	0.24
	3.0–4.76	0.78	0.58	0.42
	0.5–4.76	**0.86**	**0.64**	**0.64**
$\theta_{b,1}$	0.5–1.3	4.65	5.38	3.67
	1.3–3.0	5.13	3.35	3.40
	3.0–4.76	1.97	2.50	2.17
	0.5–4.76	**4.07**	**3.47**	**3.02**
$\theta_{b,2}$	0.5–1.3	2.61	4.93	1.68
	1.3–3.0	3.78	4.08	1.80
	3.0–4.76	2.67	5.61	4.07
	0.5–4.76	**3.20**	**4.88**	**2.92**

d. Comparison with numerical experiments

Accurate determination of the directional distribution function can be used for the verification of nonlinear wave models. For example, Banner and Young (1994) perform numerical experiments to investigate the functional forms of the wind input and wave dissipation source terms. One of the test series examines the dissipation term, which is formulated with a frequency dependence of ω^2, ω^3, or ω^4 based on the study of Komen et al. (1984) and Hasselmann (1974). The results show that the directional distribution function is very sensitive to the specification of the dissipation function. In all cases, the lobe angle increases with k/k_p, but the lobe ratio behaves very differently. For the ω^2 case, it appears to increase monotonically with k/k_p [this conclusion is tentative because results for only three different wavenumbers, $k/k_p = 1$, 4, and 9, were shown in Fig. 13 of Banner and Young (1994)]. For the other two dissipation functions, the lobe ratios at $k/k_p = 9$ are less than those at $k/k_p = 4$. Their model results are also plotted in Figs. 11c,d and 12c,d.

The ATM data shown in Figs. 10d (quasi-steady case) and 12d (decaying case) suggest a monotonic increase of the lobe ratio in the wavenumber range $1 \leq k/k_p \leq 7$. The data beyond $k/k_p > 7$ are quite scattered. We emphasize that, although the ATM data shown here extend to $k/k_p = 10$, our conservative estimate of the Nyquist wavenumber is $k_{\mathrm{Ny}}/k_p = 5$ (based on the coarsest along-track data spacing of 6 m). The spectral results in the range of $10 > k/k_p > 5$ are essentially ''push processed'' due to our choice of using square grids of 3-m size to resample the circularly scanner dataset (Part I). With this caution in mind, it is commented that the comparison of numerical results with ATM data at $k/k_p = 9$ is only tentative, more solid comparisons can only be made at a later stage when datasets extending to higher k/k_p range become available. The comparison at $k/k_p = 4$, however, should be reliable. Several conclusions can be reached at this stage. (i) The lobe angle based on the numerical simulation overpredicts the lobe spacing at $k/k_p = 4$ but it is in excellent agreement with ATM measurement at $k/k_p = 9$. (ii) Both numerical simulations and ATM measurements show that the lobe angle of the directional distribution is not sensitive to the wave conditions. Specifically, the lobe angle derived from a quasi-steady and active-growing wave field is not very different from the lobe angle obtained from a decaying wave field. (iii) In a quasi-steady wave field, the lobe ratio computed from an ω^2 dissipation function is less than the ATM observation. On the other hand, cubic and quartic dissipation functions overpredict the lobe ratio. The frequency dependence of the dissipation function appears to be between quadratic and cubic. The lobe ratios computed from the numerical model at $k/k_p = 9$ with all three frequency dependencies are significantly lower that the ATM measurements. As noted in the last paragraph, ATM data quality at $k/k_p > 5$ in this dataset is unknown and further quantitative assessment is not warranted. (iv) In the decaying case, the computation using quadratic dissipation function again underestimates the lobe ratio. Results based on cubic and quartic dissipation functions are in excellent agreement with ATM data at $k/k_p = 4$. Based on these limited data, it seems to suggest that the frequency dependence of the dissipation function is close to $\omega^{2.5}$ for a quasi-steady and active-generation wave field. For a decaying wave field, the frequency dependence is stronger. The limited data available at this stage are not sufficient to discriminate the difference between cubic and quartic computations.

Komen et al. (1984) design a sequence of numerical experiments to investigate the existence of fully developed windseas. The analysis concludes that the dissipation function with ω^2-dependence yields the most satisfying results. Both sets of numerical experiments point out that the simulated directional distributions differ from cos squared and sech squared spreading function. These numerical experiments indicate that the investigation of directional distribution enhances our understanding of the key mechanisms governing the wave dynamics, and that the information on the directional distribution serves to verify the performance of nonlinear ocean wave models.

e. Comparison with buoy measurements

Most studies on the directional distribution of ocean waves are based on temporal measurements by wave gauge arrays or directional buoys. The directional distributions derived from temporal measurements vary significantly depending on the selected analysis methods, which are quite numerous (e.g., Benoit et al. 1997). This method-dependent variation has caused significant

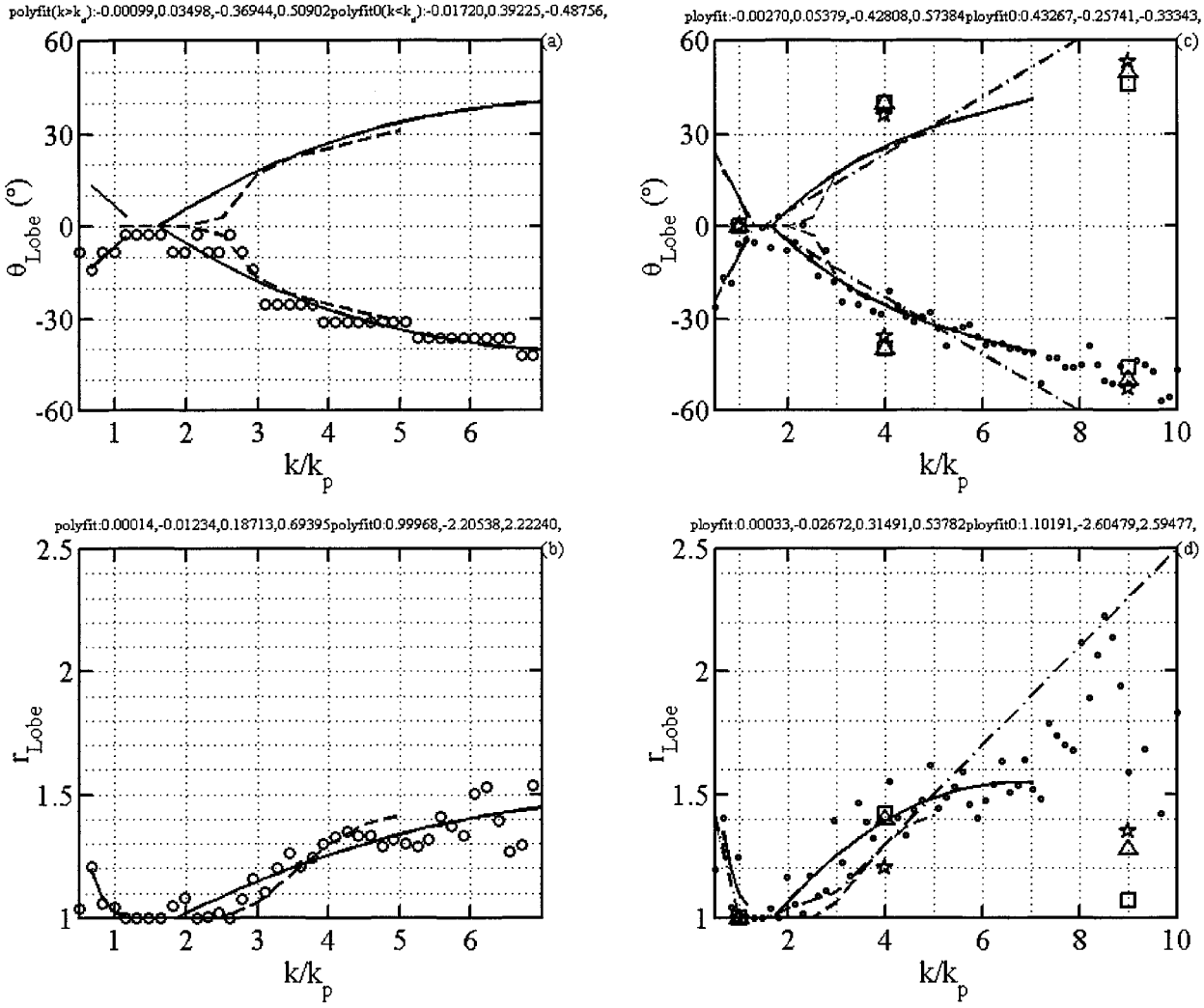

FIG. 11. As in Fig. 10 but for the decaying wave field.

difficulties in the interpretation of the directional spreading characteristics of multimodal cases. Due to the lack of independent in situ spatial measurements, comparisons and verifications of various directional analysis methods applying to temporal measurements can only be done using laboratory or numerically simulated data. These simulated data are usually quite simplified in comparison to the real ocean data.

It is of interest to compare the estimated directional distributions from buoy wave data with those derived from the 3D ocean surface topography measured by the ATM. The buoy directional distributions are extracted from the archive of the offshore NDBC pitch-roll buoy (station ID 44014). As shown in Part 1, the wind and wave conditions in the region were quasi-homogenous during the four hours of aircraft measurements. Every hour, the frequency-dependent Fourier coefficients of the first two harmonic terms in (9) are estimated from measurements of buoy heave, pitch, and roll motions. Details of buoy measurements and data processing are described in Earle (1996). For the comparison with ATM data, buoy measurements from 1300 and 1400 UTC are averaged and the Fourier coefficients are calculated from the average data. This period corresponds to the quasi-steady wave condition in the ATM data. The directional distribution at each frequency is estimated from the Fourier coefficients using the MEM (Lygre and Krogstad 1986) and the MLM (Oltman-Shay and Guza 1984). The computational resolution of the MEM and MLM directional distribution is 1°, but in reality the directional resolution of buoy measurement is considerably coarser.

The MEM has a much better directional resolving power than the MLM. It is also known that the MEM tends to overpredict the magnitude of the directional peaks and may sometimes create artificial bimodal distributions on (simulated) unimodal cases (Benoit et al. 1997; Lygre and Krogstad 1986). In addition, an em-

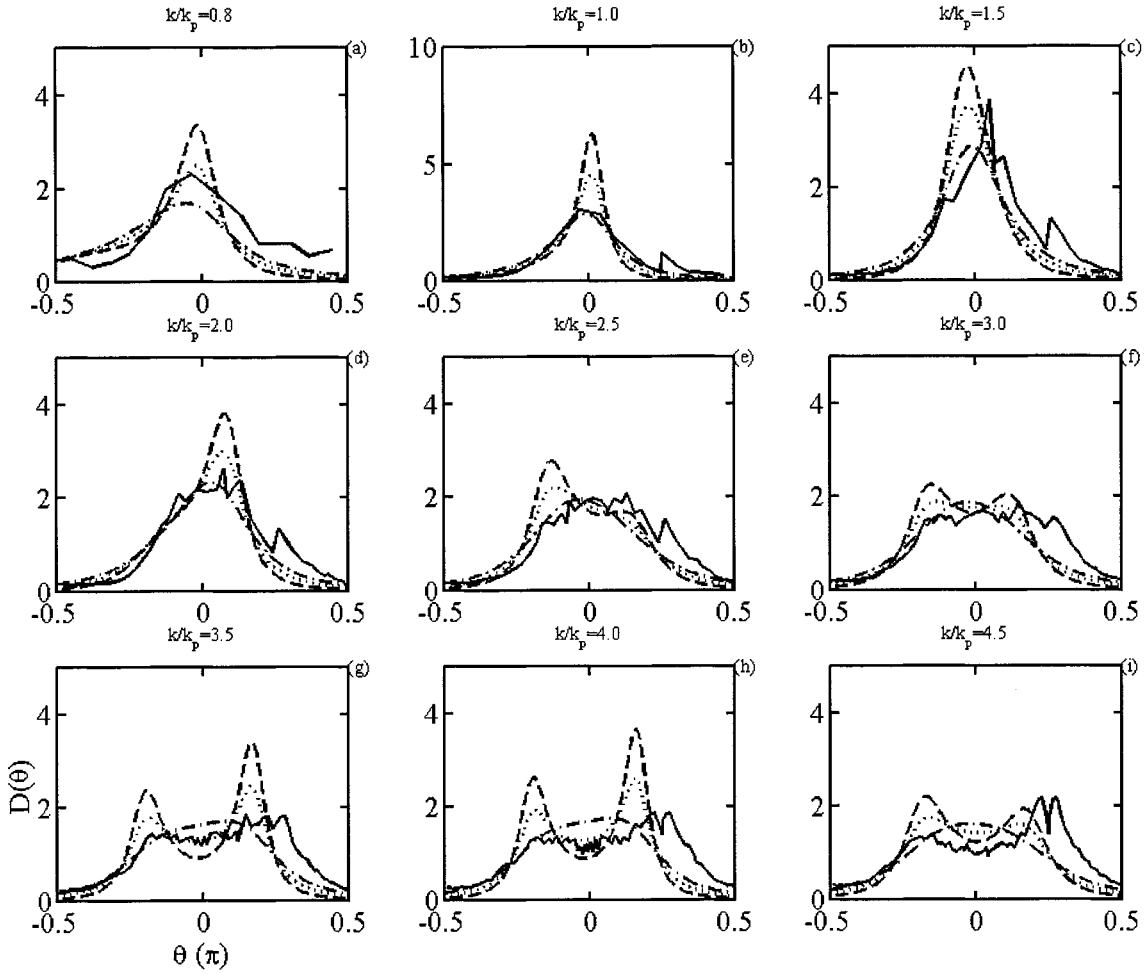

FIG. 12. Comparisons of the directional distributions from offshore buoy measurements, processed by MEM (dashed curves), MLM (dashed–dotted), and EMP (dotted), with those obtained by the ATM measurements (solid curves). Cases at nine different wavenumbers (shown on top of each panel) are illustrated.

pirical distribution defined as the average of the MEM and MLM results is used to compare with the ATM data. The empirical function is denoted as EMP. Figure 12 shows the comparison of the directional distribution of ATM data (solid line) and the estimates by MEM (dashed line), MLM (dash-dotted line), and EMP (dotted line) at nine selected normalized wavenumbers (k/k_p) from 0.8 to 4.5. The direction has been shifted such that the dominant wave direction is at 0°. At $k/k_p < 3$, there is no noticeable bimodal feature in the ATM data. The MLM estimate agrees well with the ATM data while the MEM estimate has a sharper and narrower peak than the ATM data and the MLM estimate. At $k/k_p > 3$, the bimodal feature of ATM data becomes more visible as wavenumber increases. The MEM estimate starts to show the two peaks of bimodal distribution. The peaks, however, are much sharper and higher than the ATM data. The MLM estimate remains very broad and fails to display the bimodal feature. For the bimodal cases, the EMP appears to provide a reasonable compromise between the overprediction of MEM and the coarse directional resolution of MLM.

To further quantify the comparison, the wavenumber-dependent directional parameters, $I_{D,1}$, $I_{D,2}$, $\theta_{b,1}$, and $\theta_{b,2}$, are computed from the directional distributions of the MEM, MLM, and EMP to compare with the ATM data. Figures 13a and 13b show the computed $I_{D,1}$ and $I_{D,2}$, respectively. In the region where bimodal feature is not dominant ($k/k_p < 3$), all estimates from MEM, MLM, and EMP show similar trends to the ATM data. The lowest values of the integrated distributions are consistently at around $k/k_p = 1.3$. In this region of unimodal distribution, both MEM and MLM estimates generally follow the ATM data. For $I_{D,1}$, the MLM estimate is slightly higher, and the MEM estimate is slightly lower than the ATM results. For $I_{D,2}$, the MLM estimate is in fact in excellent agreement with the ATM data. The MEM estimates show large fluctuation. When bimodality becomes apparent ($k/k_p > 3$), MEM estimates of $I_{D,1}$ differ significantly from the ATM data. The agree-

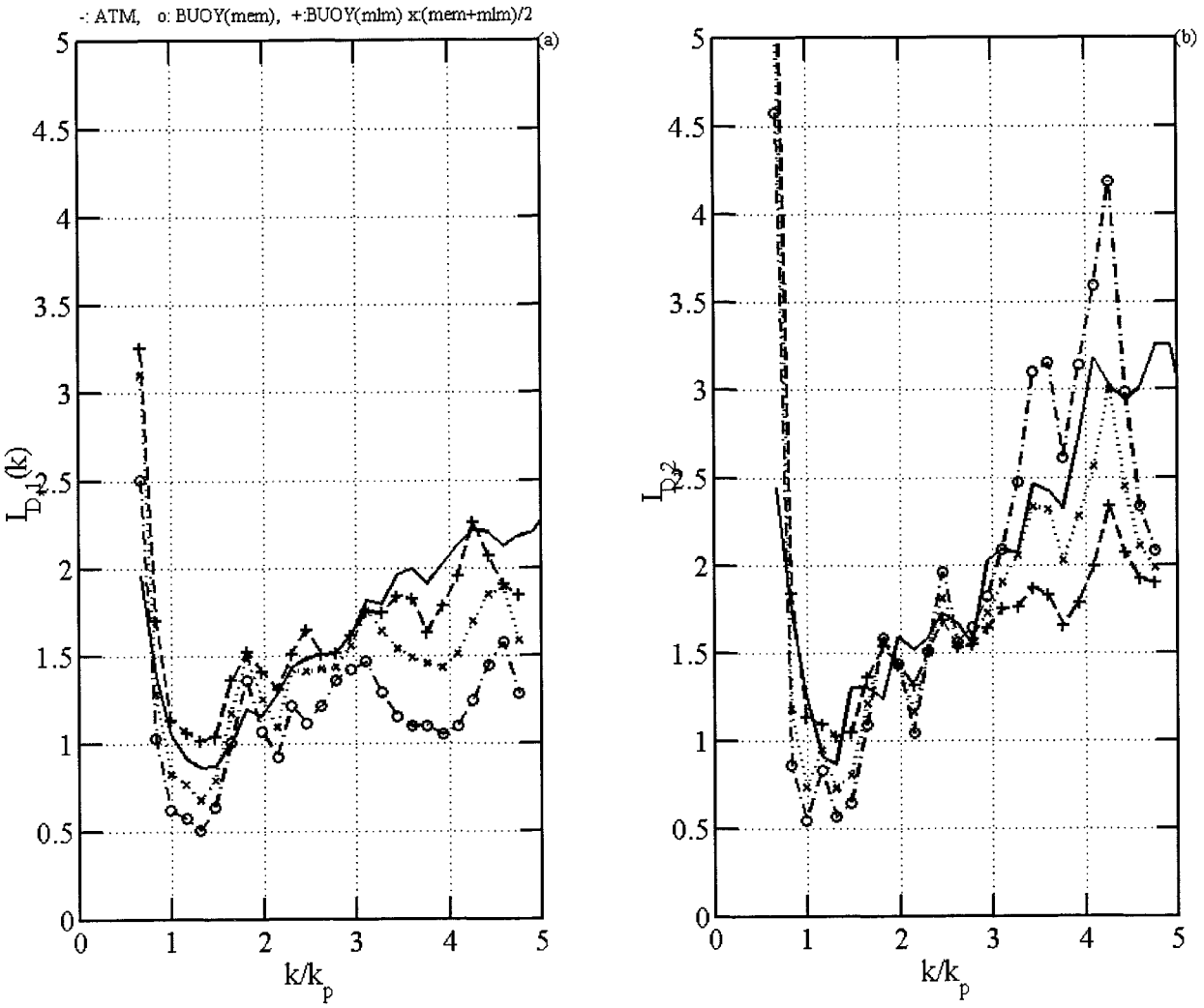

FIG. 13. ATM and buoy comparison of the integrated directional distribution (a) $I_{D,1}$ and (b) $I_{D,2}$. Solid curves: ATM, connected circles: MEM, connected pluses: MLM, and connected crosses: EMP.

ment of the MLM estimate of $I_{D,1}$ with ATM data is very good in this range, but as commented earlier, MLM fails to identify the bimodal feature in the directional distribution (Fig. 12). For the integral $I_{D,2}$, the estimates by MEM and MLM diverge from the ATM data, the agreement clearly deteriorated compared to that in the lower wavenumber range (Fig. 13b). The rms differences between ATM and MEM, MLM, or EMP estimates are listed in Table 3. Statistics in the wavenumber range (k/k_p) from [0.5, 1.3], [1.3, 3.0], [3.0, 4.76], and [0.5, 4.76] are calculated separately to provide a more detailed comparison in different wavenumber ranges. Overall, the rms differences of $I_{D,1}$ and $I_{D,2}$ between ATM and MEM data are not better than the rms differences between ATM and MLM.

Comparisons of $\theta_{b,1}$ and $\theta_{b,2}$ are shown in Fig. 14. All estimates show that the spreading width is narrowest at k/k_p, slightly larger than 1. Around $k/k_p = 1$, $\theta_{b,1}$ and $\theta_{b,2}$ of the ATM data are larger than the MEM estimates and smaller than the MLM estimates. For $\theta_{b,1}$ (Fig. 14a) the MEM estimates agree well with the ATM data. The MLM estimates have a wider spreading width than the ATM data at $k/k_p < 3$, and then become slightly narrower than the ATM data at $k/k_p > 3$. For $\theta_{b,2}$ (Fig. 14b) the MEM estimates are generally smaller than the ATM data. The MLM estimates indicate a broader spreading width compared to the ATM data in the range $k/k_p < 3$, the trend is reversed for higher k/k_p. The rms statistics on $\theta_{b,1}$ and $\theta_{b,2}$ are listed in Table 3 also. Again, the overall agreement between ATM and MEM results is not better than the agreement between ATM and MLM results. Interestingly, the empirical distribution (EMP) calculated by simply averaging the MEM and MLM results seems to provide much better overall agreement with ATM measurement.

The lobe ratio and lobe angle of MEM and EMP

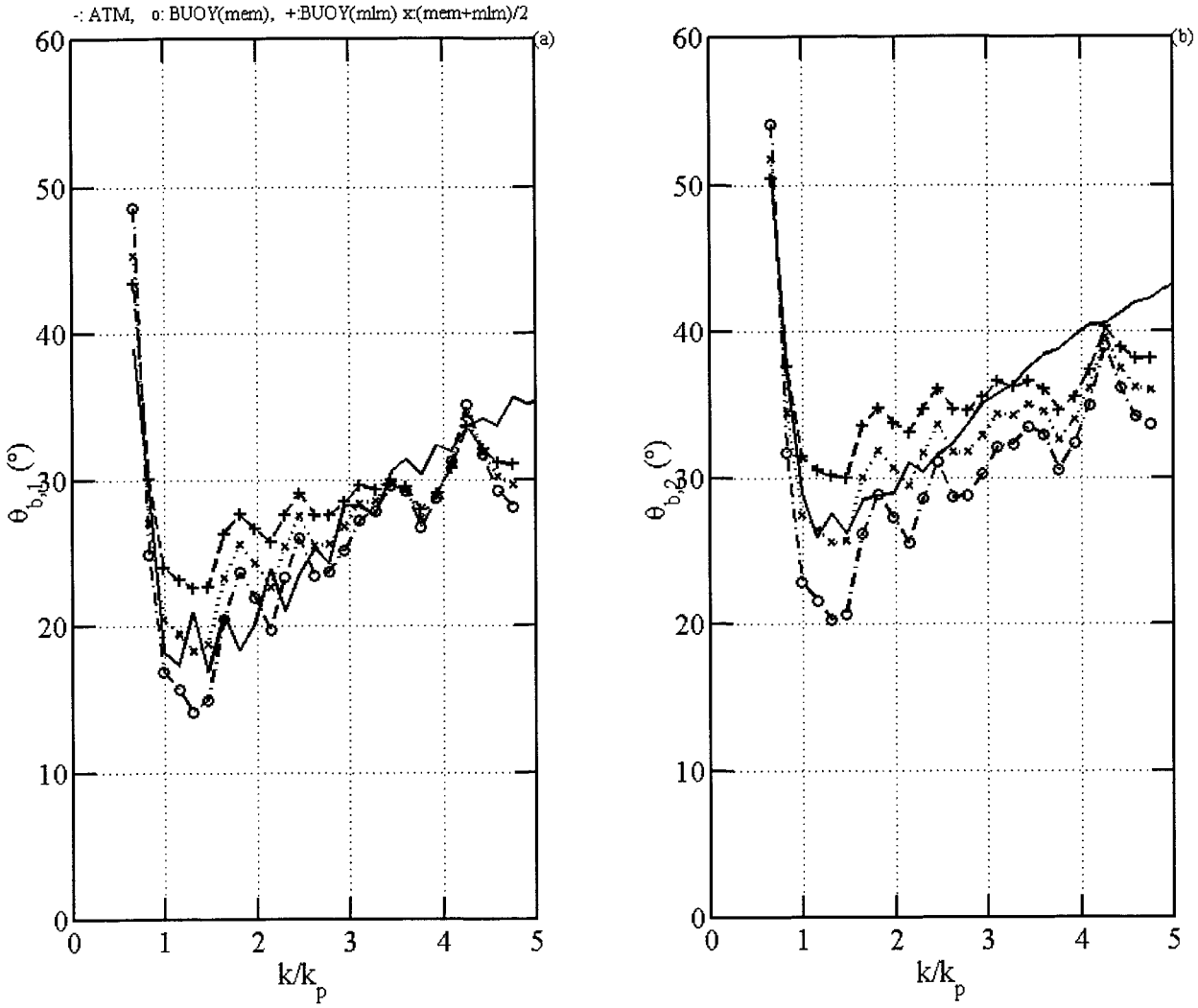

FIG. 14. ATM and buoy comparison of the directional moments (a) $\theta_{b,1}$ and (b) $\theta_{b,2}$. Solid curves: ATM, connected circles: MEM, connected pluses: MLM, and connected crosses: EMP.

estimates are compared with the ATM data (Fig. 15). The MLM estimates are not included in this comparison due to its lack of any noticeable bimodal feature. The comparisons are carried out for both the quasi-steady (Figs. 15a,b) and decaying wave fields (Figs. 15c,d). The lobe angles of both MEM and EMP estimates increase as k/k_p increases, which are consistent with the trend of the ATM data. Quantitatively, the lobe angles of the MEM and the EMP estimates are approximately 10° larger than the ATM data. The lobe ratios estimated using the MEM show very large fluctuations, especially in the region of $k/k_p > 3$, where the bimodal feature becomes prominent as observed from the ATM data. The bimodal distributions of MEM processing tend to have significant variations and the two lobes are usually unequal in magnitude and shape. They are often not symmetric with respect to the dominant wave direction. These sensitive variations are possibly MEM artifact rather than true reflection of the directional properties of wind-generated wave. The EMP, as an empirical fix, produces estimates that have a much better agreement with the ATM data.

An extensive analysis is carried out on the directional data during two active wave growth periods at two buoy stations in the Lake Michigan using the EMP method (Wang and Hwang 1999, submitted to *J. Phys. Oceanogr.*). Each growth period is longer than 12 h. The analysis shows that the bimodal directional distribution is distinctive and persistent through the wave growth process. The directional bimodality is characterized by the parameters of lobe separation angle θ_{lobe} and lobe ratio r_{lobe}. The values of the two parameters show a dependence on the normalized frequency f/f_p. Both θ_{lobe} and r_{lobe} are smallest at the peak frequency. The values of θ_{lobe} and r_{lobe} increase as wave frequency moves to both lower and higher frequencies. They also made extensive

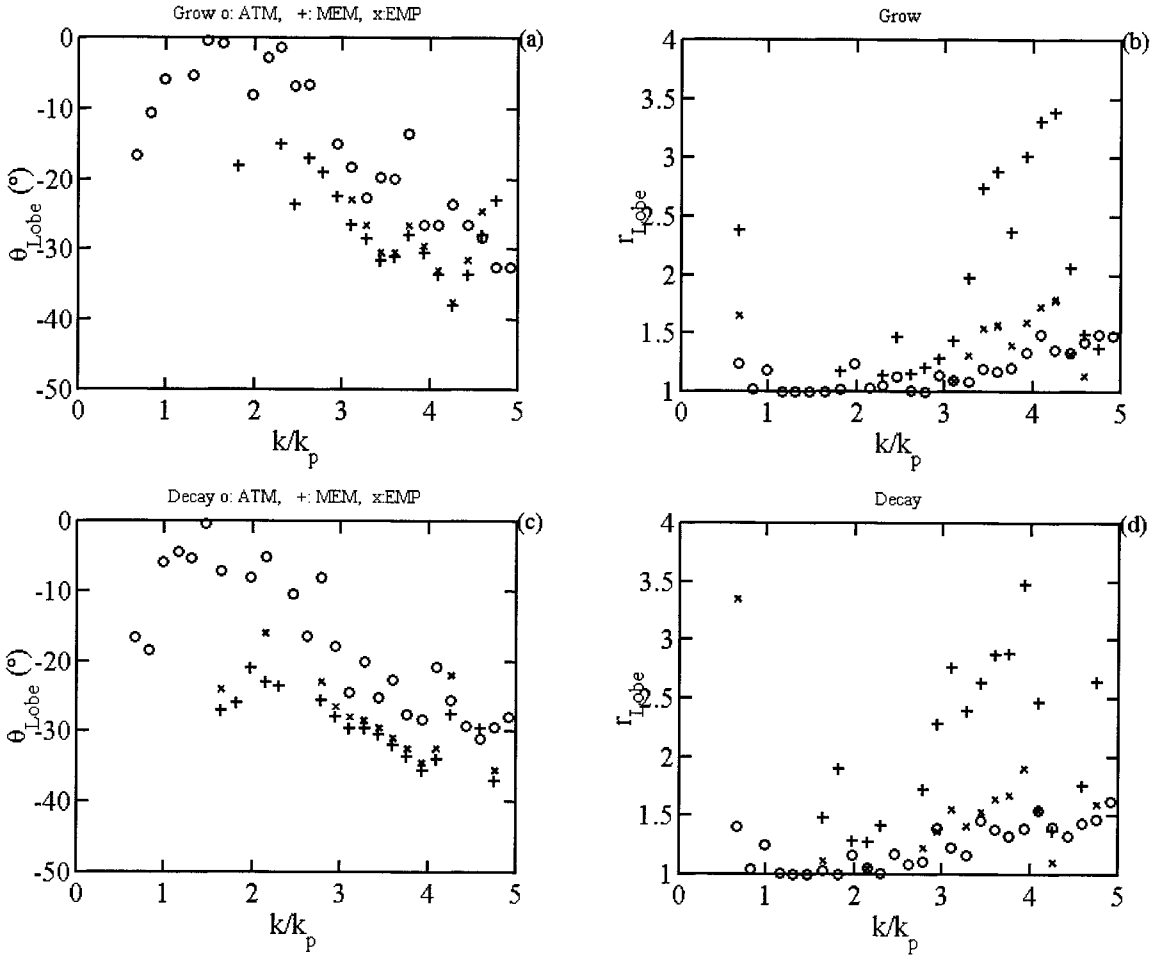

FIG. 15. ATM and buoy comparison of the lobe angle and lobe ratio for the quasi-steady wave field (a, b) and decaying wave field (c, d). The lobe angles are shown in (a) and (c), and the lobe ratios are shown in (b) and (d). Circles: ATM, pluses: MEM, and crosses: EMP.

comparisons with the results obtained from the ATM measurements, the field study of Ewans (1998) and results from nonlinear numerical model simulations (Banner and Young 1994; Young et al. 1995).

4. Summary

An airborne scanning lidar acquires high-resolution spatial measurements of the 3D topography of ocean surface waves. From these spatial data, 2D wavenumber spectra can be calculated in a straightforward fashion. These 2D wavenumber spectra have excellent directional resolution, better than 10° for wave components above k_p in the present dataset (Fig. 2). The analysis of the resulting directional distribution shows that the spreading factor is narrowest near the spectral peak wavenumber ($k_n = 1.3k_p$), and broadens toward both higher and lower wavenumbers from k_n (Figs. 9 and 10). These results are consistent with those derived from measurements using directional buoys and wave gauge arrays although the value of k_n of each dataset differs: $k_n = 0.9k_p$ in Donelan et al. (1985), $1.0k_p$ in Mitsuyasu et al. (1975), and $1.1k_p$ in Hasselmann et al. (1980).

The development of bimodal distribution is clearly shown in the 2D wavenumber spectrum obtained from the 3D surface topography. The wavenumber dependence of the lobe angle and lobe ratio is established from the present dataset (Table 2 and Figs. 10–12). Fourier decomposition of the directional distributions is performed [Eq. (8) and Fig. 6]. Coefficients of the third-order polynomial fitting of the leading nine Fourier coefficients are listed in Table 1. Compared with measured data, it is found that major features of the directional distributions such as the beamwidth (spreading factor), lobe angle, and lobe ratio can be sufficiently represented by four Fourier components of the distribution function (Figs. 7b, 7d, 8, 10, and 11).

Numerical experiments (e.g., Komen et al. 1984; Banner and Young 1994) demonstrate that the directional distribution function is sensitive to different formula-

tions of the source terms. Accurate determination of the directional distribution is needed to enhance our understanding of ocean wave dynamics and to validate the performance of nonlinear ocean wave models. The ATM results are compared with numerical experiments of Banner and Young (1994) to investigate the frequency dependence of the dissipation function. From the limited data available, it is suggested that in an active wind-generated wave field, the frequency dependence of the dissipation function is close to $\omega^{2.5}$. In a decaying wave field, the frequency dependence is stronger. Available data are not sufficient to distinguish between results calculated from ω^3 and ω^4 dissipation functions.

Finally, the ATM data are also used to investigate the performance of the MEM and MLM directional resolution. In general, the resolution of MLM is relatively poor in the case with multimodal directional distribution. On the other hand, the modal structure detected by MEM is exaggerated and the resulting spreading factor (beamwidth) is in general smaller than the ATM measurement (Figs. 13–15, Table 3). For application purposes, it is found that the empirical average (EMP) of MLM and MEM represents a working solution that results in improved agreement with the measured directional distribution from 3D surface topography.

Acknowledgments. This work is sponsored by the Office of Naval Research through Naval Research Laboratory's research project ''Phase-resolved nonlinear transformation of shoaling waves'' (Program Element 62435N) and NASA's Mission to Planet Earth. We express our appreciation of the flight crew and the engineers and technicians who successfully executed the field experiment. The in situ wind and wave data were supplied by the Field Research Facility, U.S. Army Corps of Engineers, and the National Data Buoy Center, National Oceanographic and Atmospheric Administration.

REFERENCES

Banner, M. L., 1990: Equilibrium spectra of wind waves. *J. Phys. Oceanogr.,* **20,** 966–984.

——, and I. R. Young, 1994: Modeling spectral dissipation in the evolution of wind waves. Part I: Assessment of existing model performance. *J. Phys. Oceanogr.,* **24,** 1550–1571.

Benoit, M., P. Frigaard, and H. A. Schaffer, 1997: Analyzing multidirectional wave spectra: A tentative classification of available methods. *Proc. Seminar on Multidirectional Waves and their Interaction with Structures,* San Francisco, CA, International Assembly of Hydraulic Research, 131–158.

Cote, L. J., and Coauthors, 1960: The directional spectrum of a wind generated sea as determined from data obtained by the Stereo Wave Observation Project. Meteorological Papers, Vol. 2, University Publishers Tech. Rep., New York University, 88 pp.

Donelan, M. A., J. Hamilton, and W. H. Hui, 1985: Directional spectra of wind-generated waves. *Philos. Trans. Roy. Soc. London,* **A315,** 509–562.

Earle, M. D., 1996: Nondirectional and directional wave data analysis procedures. NDBC Tech. Doc. 96-01, 37 pp. [Available from NDBC, Stennis Space Center, MS 39529.]

Ewans, K. C., 1998: Observations of the directional spectrum of fetch-limited waves. *J. Phys. Oceanogr.,* **28,** 495–512.

Hasselmann, D. E., M. Dunckel, and J. A. Ewing, 1980: Directional wave spectra observed during JONSWAP 1973. *J. Phys. Oceanogr.,* **10,** 1264–1280.

Hasselmann, K., 1974: On the spectral dissipation of ocean waves due to whitecapping. *Bound.-Layer Meteor.,* **6,** 107–127.

Holthuijsen, L. H., 1983: Observations of the directional distribution of ocean-wave energy in fetch-limited conditions. *J. Phys. Oceanogr.,* **13,** 191–207.

Hwang, P. A., E. J. Walsh, W. B. Krabill, R. N. Swift, S. S. Manizade, J. F. Scott, and M. D. Earle, 1998: Airborne remote sensing applications to coastal wave research. *J. Geophys. Res.,* **103,** 18 791–18 800.

——, D. W. Wang, E. J. Walsh, W. B. Krabill, and R. N. Swift, 2000: Airborne measurements of the wavenumber spectra of ocean surface waves. Part I. Spectral slope and dimensionless spectral coefficient. *J. Phys. Oceanogr.,* **30,** 2753–2767.

Jackson, F. C., W. T. Walton, and C. Y. Peng, 1985: A comparison of in situ and airborne radar observations of ocean wave directionality. *J. Geophys. Res.,* **90,** 1005–1018.

Komen, G. J., S. Hasselmann, and K. Hasselmann, 1984: On the existence of a fully developed wind-sea spectrum. *J. Phys. Oceanogr.,* **14,** 1271–1285.

Krabill, W. B., R. H. Thomas, K. Jezek, C. Kuivinen, and S. Manizade, 1995a: Greenland ice sheet thickness changes measured by laser altimetry. *Geophys. Res. Lett.,* **22,** 2341–2344.

——, ——, C. F. Martin, R. N. Swift, and E. B. Frederick, 1995b: Accuracy of airborne laser altimetry over the Greenland ice sheet. *Int. J. Remote Sens.,* **16,** 1211–1222.

Longuet-Higgins, M. S., D. E. Cartwright, and N. D. Smith, 1963: Observations of the directional spectrum of sea waves using the motions of a floating buoy. *Ocean Wave Spectra,* Prentice Hall, 111–136.

Lygre, A., and H. E. Krogstad, 1986: Maximum entropy estimation of the directional distribution in ocean wave spectra. *J. Phys. Oceanogr.,* **16,** 2052–2060

Mitsuyasu, H., and Coauthors, 1975: Observation of the directional wave spectra of ocean waves using a cloverleaf buoy. *J. Phys. Oceanogr.,* **5,** 750–760.

Oltman-Shay, J., and R. T. Guza, 1984: A data-adaptive ocean wave directional spectrum estimator for pitch–roll type measurements. *J. Phys. Oceanogr.,* **14,** 1800–1810.

Phillips, O. M., 1958: On some properties of the spectrum of wind-generated ocean waves. *J. Mar. Res.,* **16,** 231–240.

——, 1985: Spectral and statistical properties of the equilibrium range in wind-generated gravity waves. *J. Fluid Mech.,* **156,** 505–531.

Wyatt, L. R., 1995: The effect of fetch on the directional spectrum of Celtic Sea storm waves. *J. Phys. Oceanogr.,* **25,** 1550–1559.

Young, I. R., 1994: On the measurement of directional wave spectra. *Appl. Ocean Res.,* **16,** 283–294.

——, and G. Ph. Van Vledder, 1993: A review of the central role of nonlinear interactions in wind-wave evolution. *Philos. Trans. Roy. Soc. London,* **A342,** 505–524.

——, L. A. Verhagen, and M. L. Banner, 1995: A note on the bimodal directional spreading of fetch-limited wind waves. *J. Geophys. Res.,* **100,** 773–778.